3D Experimental Quantification of Fabric and Fabric Evolution of Sheared Granular Materials Using Synchrotron Micro-Computed Tomography

A Thesis Presented for the

Master of Science

Degree

The University of Tennessee, Knoxville

Wadi Habeeb Imseeh

December 2017

ACKNOWLEDGEMENTS

I would like to express my sincere gratitude to my advisor Prof. Khalid Alshibli, the Department of Civil and Environmental Engineering, the University of Tennessee-Knoxville (UTK). Prof. Alshibli has always been a source of motivation, enthusiasm, and immense Knowledge. His guidance and insights provided me with continual support that inspired this final product. I would also like to thank Prof. Angel Palomino and Prof. Timothy Truster for serving on my MS thesis committee and acknowledge Dr. Andrew Druckrey who was my former colleague in our research team at UTK. This thesis was completed as an extension of his PhD dissertation work.

This material is partially funded by the US National Science Foundation (NSF) under Grant No. CMMI-1266230 and Office of Naval Research (ONR) grant No. N00014-11-1-0691. Any opinions, findings, and conclusions or recommendations expressed in this material are those of the authors and do not necessarily reflect the views of the NSF or ONR. We used resources of the Advanced Photon Source (APS), a U.S. Department of Energy (DOE) Office of Science User Facility operated for the DOE Office of Science by Argonne National Laboratory (ANL) under Contract No. DE-AC02-06CH11357. The SMT images presented in this thesis were collected using the x-ray Operations and Research Beamline Station 13-BMD at Argonne Photon Source (APS), ANL. We thank Dr. Mark Rivers of APS for help in performing the SMT scans. We also acknowledge the support of GeoSoilEnviroCARS (Sector 13), which is supported by the National Science Foundation, Earth Sciences (EAR-1128799), and the DOE, Geosciences (DE-FG02-94ER14466).

ABSTRACT

Many experimental studies have demonstrated that mechanical response of granular materials is highly influenced by micro-structural fabric and its evolution. In the literature, quantification of fabric and its evolution has been developed based on micro-structural observations using Discrete Element Method (DEM) or 2D experiments with simple particle shapes. The emergence of x-ray computed tomography (CT) technique has made quantification of such experimental micro-structural properties possible using 3D high-resolution images. Synchrotron micro-computed tomography (SMT) was used to acquire 3D images during in-situ conventional triaxial compression experiments on granular materials with different morphologies. 3D images were processed to quantify fabric and its evolution based on experimental measurements of contact normal vectors between particles. Overall, the directional distribution of contact normals exhibited the highest degree of isotropy at initial configuration (i.e., zero global axial strain). As compression progressed, contact normals evolved in the direction of loading until reaching a constant fabric when experiments approached the critical state condition. Further assessment of the influence of confining pressure, initial density state, and particle-level morphology on fabric and its evolution was formed. Results show that initial density state and applied confining pressure significantly influence the fabric-induced internal anisotropy of tested specimens at initial configurations as well as the magnitude of fabric evolution throughout triaxial compression experiments. Relatively, a higher applied confining pressure and a looser initial density state resulted in a higher degree of fabric-induced internal anisotropy. Influence of particle-scale morphology was also found to be significant particularly on fabric evolution.

TABLE OF CONTENTS

LIST OF TABLES

LIST OF FIGURES

CHAPTER ONE: INTRODUCTION AND GENERAL DESCRIPTION

A version of this thesis is currently under review for publishing by Wadi H. Imseeh, Andrew M. Druckrey, and Khalid A. Alshibli:

Imseeh, W. H., Druckrey, A. M., and Alshibli, K. A. (2017). "3D Experimental Quantification of Fabric and Fabric Evolution of Sheared Granular Materials Using Synchrotron Micro-Computed Tomography." *Granular Matter*, Under revision.

This paper has been submitted to Granular Matter journal and is currently under review. In this work, I have completed image pre-processing of all 3D scans using AVIZO 9.4 software. I have also completed image processing by executing a C++ code version that was originally developed by Riyadh I. Al-Raoush and Andrew M. Druckrey. I also generated all figures related to fabric by developing MATLAB codes in collaboration with my former colleague in our research team Andrew M. Druckrey. Wadi H. Imseeh and Andrew M. Druckrey co-wrote the paper, Khalid A. Alshibli finalized and submitted the paper. The experimental work and SMT scanning was completed by the combined effort of Andrew M. Druckrey and Khalid A. Alshibli.

Introduction

Micro-scale properties and particle-to-particle association of granular materials contribute to their macroscopic strength and dilatancy behavior as well as other engineering properties. Fabric or internal structure is broadly defined as the arrangement of particles, particle groups, and associated pore spaces. In the last few decades, numerous experiments and discrete element models have demonstrated that mechanical properties of granular material are remarkably influenced by fabric-induced internal anisotropy. To mention few examples, Oda (1972) investigated fabric of various sands using 2D thin section microscopy technique to conclude that differences in fabric significantly influence mechanical properties and specimens with preferential orientation of contact normals toward the direction of loading have a more stable fabric. Lam and Tatsuoka (1988) studied the influence of initial fabric on strength and deformation characteristics of air-pluviated Toyoura sand based on drained tests in triaxial compression, triaxial extension, and plane strain compression. Bathurst and Rothenburg (1990) presented a series of theoretical developments and numerical experiments directed at quantifying important features of the micro-mechanical behavior of granular media by introducing average characteristics of fabric anisotropy. Jang and Frost (2000) used digital image analysis to examine particle orientations in local shear zones of sand tested under conventional triaxial compression. Yimsiri and Soga (2001) simulated the undrained behavior of sands in monotonic triaxial compression and extension to assess the effect of initial fabric on the undrained shear strength. Li and Dafalias (2000) proposed a theory within the framework of critical state soil mechanics for cohesionless soils and later developed the Anisotropic Critical State Theory (ACST) (Dafalias 2016; Dafalias and Manzari 2004; Li and Dafalias 2011; Li and Dafalias 2002; Theocharis et al. 2016) which incorporates fabric as a state parameter that describes the internal anisotropy of granular materials. Ng (2009) examined three microscopic parameters (i.e., particle orientation, branch vector, and contact normal vector) at critical state of cubical triaxial specimens consists of ellipsoidal particles using DEM simulations. At critical state, the long axes of most ellipsoids were found to be perpendicular to the direction of major principal stress, the distribution of branch vectors was random, and the distribution of contact normals showed a concentration along the major principal stress direction. Guo and Stolle (2005) suggested that the shear resistance of granular materials consists of two components that are related to fabric anisotropy and inter-particle friction. Yang et al. (2008) used an image-analysis-based technique and an appropriate mathematical approach to measure inherent fabrics of sand specimens and investigate its effect on granular soil response. Yimsiri and Soga (2010) used DEM to show that initial fabric has significant effects on stiffness, strength, and dilation properties of granular materials. Li and Zeng (2014) used experimental bender element technique to confirm that morphology and density are major factors that highly influence fabric anisotropy which affects the shear modulus of the granular assembly. Guo (2014) examined the coupled effects of capillary suction and fabric-induced internal anisotropy on the behavior of partially saturated granular materials. Tong et al. (2014) experimentally evaluated the effect of bedding plane inclination angle (φ), which is a way to characterize fabric-induced internal anisotropy, on the peak friction angle (ϕ_p) of sand. Winters et al. (2016) investigated the influence of soil fabric on Mohr-Coulomb strength of cohesionless silty sand and reported that fabric has a primary influence on the global shear resistance of cohesionless soil media. Although the importance of initial fabric and its evolution resulting from particle deposition, morphology, and applied loadings is well documented in the literature, they remain difficult to effectively characterize and quantify experimentally in 3D.

As effects of fabric anisotropy on mechanics of granular material was emphasized, several studies were directed to characterize and quantify fabric in random granular assemblies. Fabric of granular material was early characterized using scaler parameters such as coordination number, distribution of void ratio, contact index, etc. (Kahn 1956; Smith et al. 1929; Taylor 1950). However, a comprehensive understanding of micro-structural geometric arrangement as well as fabric-induced internal anisotropy of granular assemblies requires the consideration of directional characterization parameters rather than scaler parameters. Examples of directional measurements of fabric commonly used in granular material are: orientations of contact normal vectors, particle long-axis, void vectors, and branch vectors (Bathurst and Rothenburg 1990; Calvetti et al. 1997; Field 1963; Mehrabadi and Nemat-Nasser 1981; Mehrabadi et al. 1982; Oda 1977; Oda and Konishi 1974). The distribution of such directional data can be qualitatively described using 2D rose diagrams (Druckrey et al. 2016) or 3D spherical histograms (Jiang and Shen 2013). Yet, for fabric-induced internal anisotropy to be incorporated as a state parameter in theories and constitutive modeling of granular material, quantitative measurements of fabric are required. In general, the distribution of any directional data is numerically characterized by what is known as fabric tensor. Accordingly, several tensorial formulations were reported in the literature to numerically quantify fabric of random granular assemblies. For example, Oda et al. (1982) introduced several measurements of fabric in random assemblies of spherical granules. In particular, a second-order symmetric tensor emerged from these measurements, which found to be of fundamental importance for the description of fabric and closely related to the distribution of contact normals in the assembly. Kanatani (1984) proposed a framework to quantify the 2^{nd} and 4^{th} order fabric tensors of the first, second, and third kind. They are symmetric tensors that numerically describe the micro-structural anisotropy of any directional data of interest in a granular media. Kanatani (1984) also reported that 4^{th} order tensors better describe material anisotropy than 2^{nd} order tensors. However, difficulties in calculating and analyzing 4^{th} order fabric tensors and their dependency on the orientation of reference coordinate system limits their use in the literature (Fu and Dafalias 2015; Theocharis et al. 2014). Iwashita and Oda (1999) introduced a fabric tensor to characterize the spatial distribution of microscopic quantities such as contact normals and particles orientation in granular media. Fonseca et al. (2013) terminated triaxial experiments at different axial strain levels and impregnated the specimens with epoxy resin. Cores were then extracted from several locations within the specimens and CT scans were acquired to quantify and compare micro-structural data distribution using rose diagrams and eigenvalue analysis. Li et al. (2009) developed a new anisotropic fabric tensor based on void cells that was well correlated with the macro behavior of granular material via numerical simulations and stated that it is a more effective definition than those based on particle orientations or contact normals. Researchers have found a strong correlation between fabric tensors based on contact normals and void space vectors (Fu and Dafalias 2015; Theocharis et al. 2014). Fabric tensors based on contact normals have the disadvantage of being difficult to accurately quantify experimentally (Theocharis et al. 2014). However, forces transmit through a mass of granular media via contacts and force chains (e.g., (Oda et al. 2004; Peña et al. 2009; Peters et al. 2005; Tordesillas and Muthuswamy 2009); therefore, accurate experimental measurement of fabric tensors based on contact normals would prove more valuable for micro-mechanics constitutive models. In summary, formulations of fabric tensors in granular materials has not been consistent in the literature, but generally attempts to quantify internal fabric resistance to loading with fabric direction and magnitude relative to the global stress direction applied at specimen boundaries (e.g., (Barreto et al. 2009; Fonseca et al. 2013; Fu and Dafalias 2015; Li and Dafalias 2011; Theocharis et al. 2014; Zhao and Guo 2013).

As fabric-induced internal anisotropy within granular materials has been numerically quantified using tensorial formulations, it has been adopted as a state parameter into several constitutive models and theories to enhance prediction of granular material response under different loading paths. To list a few examples of such studies, Tobita (1989) developed a constitutive equation associated with deformation and failure features of granular materials. The constitutive relationship was developed taking into account fabric tensor as an internal variable. Nemat-Nasser (2000) developed a robust micro-mechanically based constitutive model that accounts for pressure sensitivity, friction, dilatancy, fabric, and fabric evolution. Model parameters were estimated in Nemat-Nasser and Zhang (2002) based on the results of cyclic shearing experiments and were then used to predict other experimental results with adequate correlation. Wan and Guo (2004) incorporated fabric, as a 2^{nd} order tensor, into the stress-dilatancy equation obtained from a microscopic analysis of an assembly of rigid particles. Zhu et al. (2006) included the effects of fabric and its evolution into the dilatant double shearing model proposed in (Mehrabadi and Cowin 1978) in order to capture the anisotropic behavior and the complex response of granular assemblies in cyclic shear loading. Zhao and Guo (2013) used DEM to identify a unique property associated with fabric structure relative to stresses at critical state. A relationship between the mean effective stress and a fabric anisotropy parameter (K) was defined by the first joint invariant of the deviatoric stress tensor and the deviatoric fabric tensor. The proposed relationship was found to be unique at critical state regardless of the stress path. Qian et al. (2013) applied DEM to investigate the change of anisotropic density distributions of contact normals in a granular assembly during the course of simple shear. On the basis of microscopic anisotropy characteristics, an analytical approach was developed to explore the macroscopic behavior involving anisotropic shear strength and anisotropic stress-dilatancy. This emphasized that under shear loading, anisotropic shear strength arises primarily due to the difference between principal directions of the stress and fabric.

Objective

Theoretical values of fabric and fabric evolution were assumed and adopted in the current literature based on rudimentary experimentation or DEM with no 3D experimentally-quantified fabric tensors to validate. This thesis presents 3D experimental measurement of fabric and its evolution for a series of conventional triaxial compression experiments on granular materials of different morphologies. SMT scanning technique was employed to experimentally measure 3D contact normals to be used as the directional data of interest that describes fabric-induced internal anisotropy in granular assemblies. Accordingly, fabric tensors were constructed based on the framework proposed by Kanatani (1984). Fabric and its evolution for a typical experiment was fully presented and discussed. The influence of initial density state, confining pressure, and particle morphology on fabric and its evolution was also assessed. Results of this study can be used to formulate and validate constitutive models that incorporates theoretical fabric and fabric evolution. To the author's best knowledge, no other research of this kind is reported in the literature to supplement the models. 4^{th} order fabric tensors were also evaluated and compared to 2^{nd} order tensors that are commonly used in granular material research and modeling.

Description of Tested Materials

Three silica sands known as F-35 Ottawa sand (labeled as F35), GS#40 Columbia grout (labeled as GS40), and #1 dry glass sand (labeled as DG), were used in this study. They are silica sands with different morphology ranging from rounded to angular particles. Glass beads (labeled as GB) were also tested in this study to provide baseline measurements for roundness, sphericity, and smooth surface texture. Tested sands and glass beads were sieved between US sieves #40 (0.429 mm) and #50 (0.297 mm) to obtain a uniform grain size distribution for all tested materials. Properties of tested materials are summarized in Table 1 including void ratio limits and particle-level morphology (i.e., sphericity and roundness). Maximum void ratio (e_{max}) was measured based on ASTM D 4253 while minimum void ratio was evaluated using air pluviation which surprisingly produced denser states than the vibrating table recommended by ASTM D 4254. Average sphericity and roundness were quantified using I_{sph} and I_R indexes, respectively, as described in (Alshibli et al. 2014). For example, glass beads have an average sphericity index ($I_{sph} = 1.096$) and roundness index ($I_R = 0.965$) closest to unity (i.e., closest in shape to a sphere). F35 sand has the highest sphericity index ($I_{sph} = 1.872$) which indicates higher non-spherical shape; therefore; higher degree of interlocking between particles. DG ($I_{sph} = 1.704$) and GS40 ($I_{sph} = 1.674$) are classified to have close sphericity indexes which are closer to unity than F35 sand (i.e., more spherical). Overall, the three sands have similar average roundness indexes between 0.92 and 0.97.

Table 1. Properties of tested materials

Material/ Property	Glass Beads (GB)	F-35 Ottawa (F35)	#1 Dry Glass (DG)	GS#40 Columbia Grout (GS40)
G_s	2.55	2.65	2.65	2.60
d_{50} (mm)	0.36	0.36	0.36	0.36
C_u	1.2	1.2	1.2	1.2
C_c	0.97	0.97	0.97	0.97
e_{min}	0.554	0.490	0.626	0.643
e_{max}	0.800	0.763	0.947	0.946
I_R	0.965	0.959	0.937	0.924
I_{sph}	1.096	1.872	1.704	1.674
Source	Soda lime glass	Ottawa, IL, USA	Berkeley Springs, WV, USA	Columbia, SC, USA
Supplier	Jaygo	US Silica Company		
Grain Size Distribution	Size fraction between US sieves #40 (0.42 mm) and #50 (0.297 mm)			

Description of Testing Apparatus

A miniature apparatus was especially fabricated to conduct conventional triaxial compression experiments on cylindrical sand-size granular material specimens measuring around 10 mm in diameter and 20 mm in height. It is light in weigh and small in size apparatus to facilitate accessibility on SMT scanner. The miniature apparatus was mounted on the SMT scanner stage via a pin connection which allowed free rotation to acquire 3D scans. The miniature apparatus was designed to host a triaxial cell with capabilities similar to a conventional one. A stepper motor was attached to the triaxial cell top and used to apply displacement controlled axial load. The stepper motor provided measurements of axial displacement and a load cell was used to measure applied axial load. Load-displacement measurements were collected and recorded via a data acquisition system with a computer interface.

Specimens' Preparation

To prepare a specimen, a latex membrane, measuring 10.3 mm in outer diameter and 0.3 mm in thickness, was stretched around a specially-designed split aluminum-mold that is capable to apply vacuum pressure on the interface of the membrane-mold to properly align the membrane along the inside mold wall. Sand or glass beads were then poured through a plastic funnel in which the drop height was controlled to obtain a desired initial density. After filling the mold, the top endplate was placed on the top of the specimen, then the membrane was stretched around the top endplate and secured using an O-ring. The vacuum was released at mold-membrane interface and the split mold was removed. The test cell was assembled and pressured air was used to apply confining pressure. A constant confining pressure was maintained throughout the experiment.

Experiments and Image Acquisition

The miniature triaxial apparatus was mounted on beamline 13BMD of Advanced Photon Source (APS), Argonne National Laboratory (ANL), Illinois, USA. This SMT facility provides intense, monochromatic, continuous, and highly collimated beams of x-ray with energy ranges from 10 eV to 100 eV; therefore, the beam can provide high-resolution 3D images. Ten conventional triaxial compression experiments were conducted at various initial density states and confining pressures on tested materials as summarized in Table 2. Initial scan was acquired after applying confining pressure (σ_3) followed by multiple scans at multiple axial strains. The experiments were paused at certain axial strains to collect 900 radiograph images at 0.2° rotation increments for each scan. Radiographs were then reconstructed to create 3D SMT images with an excellent spatial resolution as summarized in Table 2. Figure 1 illustrates a schematic of experimental setup including the miniature apparatus and the SMT scanner.

Table 2. Summary of SMT scans and experiments

Material	Experiment Label	Initial void ratio (e)	σ_3 (kPa)	D_r* (%)	Scan acquired at axial strains (%)	Resolution (μm/voxel)
F-35 Ottawa sand (F35)	F35_MD_15	0.598	15	60	0.0, 1.0, 2.0, 3.6, 5.1, 7.1, 9.2, 12.1 15.8, 19.9, 22.9	8.16
	F35_D_15	0.535	15	83	0.0, 1.0, 2.0, 3.5, 5.0, 6.94, 8.9, 11.9, 17.4, 22.3	11.14
	F35_D_400	0.516	400	90	0.0, 1.0, 2.0, 3.4, 4.9, 6.9, 8.9, 11.8, 17.2	11.18
#1 Dry glass sand (DG)	DG_MD_15	0.770	15	55	0.0, 1.0, 2.0, 3.6, 5.1, 7.2, 9.2, 12.3, 15.8, 19.9	8.16
	DG_D_15	0.718	15	71	0.0, 2.0, 3.5, 5.0, 6.9, 8.9, 11.9, 17.4	11.14
	DG_D_400	0.725	400	69	0.0, 1.0, 2.0, 3.5, 5.0, 6.9, 8.9, 11.9, 17.4	11.18
GS#40 Columbia grout sand (GS40)	GS40_D_15	0.712	15	77	0.0, 1.0, 2.0, 3.5, 5.0, 7.0, 9.0, 12.0, 17.5	11.14
	GS40_D_400	0.689	400	85	0.0, 1.0, 1.9, 3.3, 4.7, 6.7, 8.6, 11.4, 14.7	8.16
Glass beads (GB)	GB_D_15	0.554	15	100	0.0, 1.0, 2.0, 3.6, 5.1, 7.1, 9.2, 12.2	11.14
	GB_D_400	0.568	400	99	0.0, 1.0, 2.1, 3.7, 5.2, 7.3, 9.4, 12.5, 18.3	11.18

*D_r = Relative Density = $\frac{e_{max}-e}{e_{max}-e_{min}}$

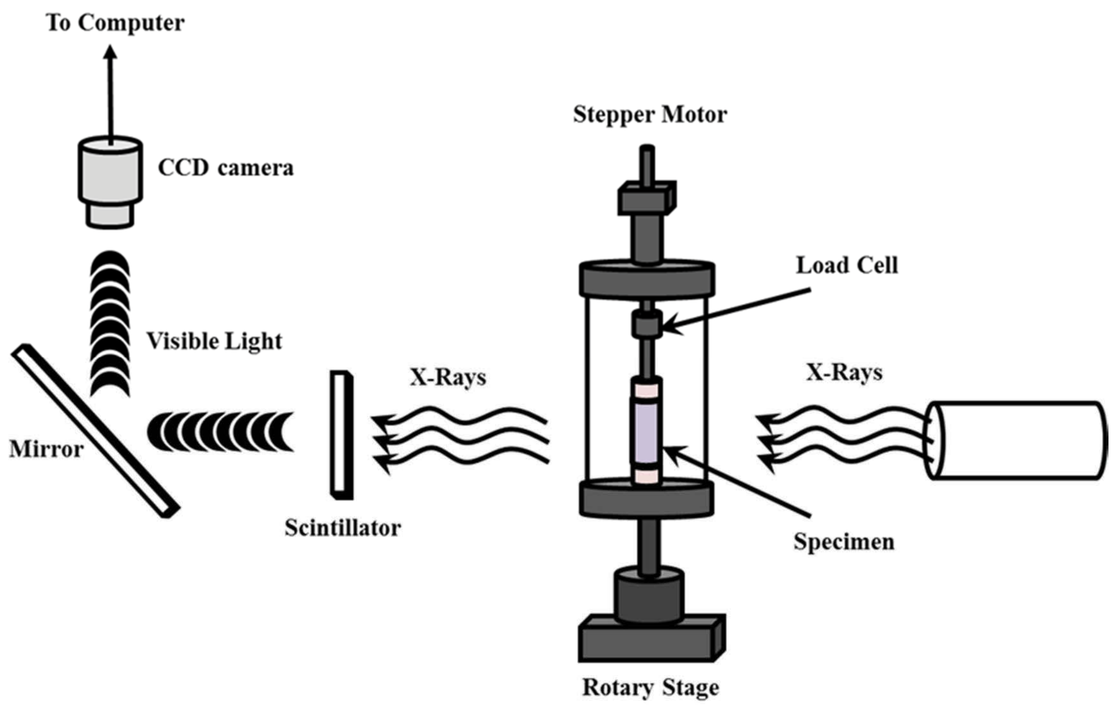

Figure 1. Schematic of the experimental setup including the miniature apparatus and SMT scanner.

SMT has proven to be a powerful non-destructive imaging technique that can be used to visualize the internal structure of granular materials. It is a technique wherein an x-ray beam passes through a specimen while attenuating. Specimen is rotated at small angular increments to produce the equivalent of a slice through the scanned specimen. the attenuated x-ray is collected by detectors and analyzed using a computer program to build a 3D image of the scanned object. A major improvement to conventional x-ray tomography systems is the incorporation of synchrotron radiation source to generate higher energy beams, around 10^6 times the energy generated using a conventional x-ray beam. The synchrotron radiation source enhancement adds several advantages on the conventional x-ray sources, including a higher photon flux (number of photons per second), higher degree of collimation (divergence of source increases image blur), and the ability to tune the photon energy over wide range using an appropriate monochromator for obtaining specific-element measurements (Kinney and Nichols 1992). Moreover, SMT scanning provides a crisp border between solids and air, which is useful in image processing. For More information on image collection and reconstruction refer to Rivers et al. (2010) and Rivers (2012).

CHAPTER TWO: QUANTIFICATION OF FABRIC AND FABRIC EVOLTION

Extracting Micro-Structural Directional Data

Acquired SMT images were pre-processed using AVIZO Fire 9.4 software. Firstly, an anisotropic diffusion filter was executed on greyscale images to reduce image noises. Filtered gray scale images were then binarized using an interactive thresholding module in which voxels belonged to solid phase were assigned a value of 1 and voxels belonged to air phase were assigned a value of 0. Afterwards, particles were separated from each other and a unique numerical label was assigned for each particle. Specimens contained between 25,000 to 50,000 particles depending on tested material and initial density state. Failure via a single well-defined shear band was observed in pre-processed scans for F35_D_400, GB_D_400 and GS40_D_400. Experiment DG_D_400 as well as all experiments with $15\,kPa$ confining pressure exhibited bulging failure which has been investigated in Amirrahmat et al. (2017) to be an external manifestation of internal shearing along multiple micro shear bands. Figure 2 illustrates a typical example of pre-processed 3D images for F35_D_400 experiment including scans acquired at all loading stages. Pre-processed labeled images were then processed using a special code that produces micro-structural data of particle lengths (short, intermediate, and long axes), volume, surface area, orientation, coordination number, contact locations, contact normal vectors, and contact tangent vectors for each particle in the entire specimen. The special computer code executes two main ‘loops’ one to define individual particle properties followed by a second loop to define contact properties. Contacts between particles are not always defined by a single continuous surface. Complex morphology and surface roughness can lead to several contact points, especially in a very angular or rough material. The special executed code implements a statistical analysis technique on contact voxels using Principal Component Analysis (PCA) to determine contact orientation (i.e., normal vector and tangential plane). Refer to Druckrey et al. (2016) for more details on the special executed code.

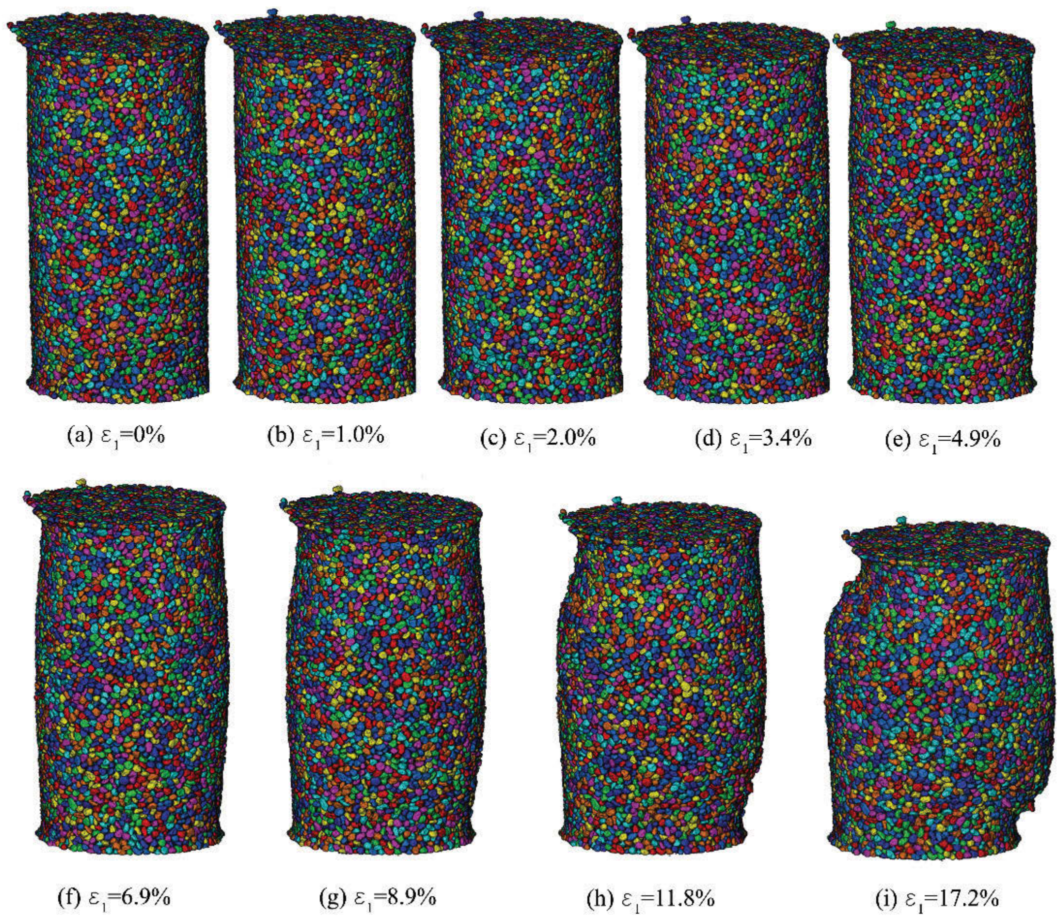

Figure 2. Processed 3D images for F35_D_400 experiment at all loading stages (ε_1 refer to the global axial strain).

The distribution of contact normal vectors has been extensively used in the literature to quantify fabric. Transmission of forces occurs through contacts and is commonly associated with stiffness and strength (Kuhn et al. 2015). Therefore, 3D unit contact normal vectors, quantified with x, y, and z components, were considered for fabric quantification. Contact normals were plotted in 3D spherical histograms to qualitatively visualize preferential orientation of internal fabric. As demonstrated in (Druckrey et al. 2016), histograms of contact normals showed a greater degree of anisotropy than branch vectors and exhibited a higher degree of evolution throughout triaxial compression experiments. In addition, force transmission through contacts in granular materials justifies the implementation of contact normals as the desirable parameter to quantify fabric for constitutive models that incorporate particle-scale properties.

Formulation of Fabric Tensors

Kanatani (1984) proposed a framework to quantify fabric tensors of any micro-structural directional data. This thesis adopted Kanatani (1984) framework with contact normals as the directional data of interest. Fabric tensor of the first kind ($N_{i_1 i_2 \dots i_r}$), also known as moment tensor, is conventionally constructed by averaging the tensorial product of contact normals:

$$N_{i_1 i_2 \dots i_r} = \frac{1}{N} \sum_{\alpha=1}^{N} n_{i_1}^{\alpha} n_{i_2}^{\alpha} \dots n_{i_r}^{\alpha} \tag{1}$$

where n_i^{α} is the α^{th} contact normal vector, *N* is the number of contacts, and *r* is the order of the tensor. Moment tensor is a symmetric tensor that interprets the relevant directional information in a tensorial structure; therefore, it plays a fundamental role in deriving further tensorial quantities that characterize the microstructural directional data distribution. However, the intuitive meaning of moment fabric tensor remains vague. Consequently, Kanatani (1984) introduced the distribution density term in order to estimate the fabric tensor of the second kind which can better interpret the microstructural directional data distribution. Let $f(\mathbf{n})$ be the empirical distribution density of contact normals in 3D, which can be expressed as:

$$f(\mathbf{n}) = \frac{1}{N}\sum_{\alpha=1}^{N} \delta(\mathbf{n} - \mathbf{n}^{(\alpha)}) \qquad 2$$

Where $\delta(\mathbf{n} - \mathbf{n}^{\alpha}) = \delta\big(\theta - \theta^{(\alpha)}\big)\delta(\phi - \phi^{(\alpha)})/\sin\theta^{(\alpha)}$, in which $\delta(*)$ is the Dirac delta function, and θ and ϕ are the spherical coordinates of the contact normal unit vector in 3D space. For example, the contact normal unit vector $\mathbf{n}^{\alpha}$ can be expressed in terms of (x, y, z) in the Cartesian Coordinate System as $(\sin\theta^{(\alpha)}\cos\phi^{(\alpha)}, \sin\theta^{(\alpha)}\sin\phi^{(\alpha)}, \cos\theta^{(\alpha)})$. Contact normals exist in pairs of unit vectors that are equal in magnitude and opposite in direction. This implies symmetry on the empirical distribution density function about the origin such that $f(\mathbf{n}) = f(-\mathbf{n})$. Moreover, the empirical distribution density function must sum up to one on a unit surface (i.e., $\int_0^{\pi}\int_0^{2\pi} f(\mathbf{n})\sin\theta\, d\phi d\theta = 1$). The empirical distribution density functions $f(\mathbf{n})$ are characterized as singular functions which limit their implementation in theories and models. Thus, several smooth distribution density functions $F(\mathbf{n})$ have been introduced in the literature to approximate the singular empirical distribution density function $f(\mathbf{n})$ (e.g., polynomial approximation, exponential approximation, etc.). In general, the approximation of a smooth density distribution function is determined by first assuming a parametric formula that involves several coefficients and then introducing a term that measures the distance between the empirical and approximated functions. Accordingly, the coefficients of the parametric formula are computed in a way that the introduced measure of distance is minimized. In this study, a polynomial in **n** approximation was implemented and the least square error criterion was used to minimize the distance between approximated and empirical functions as:

$$Er = \int [F(\mathbf{n}) - f(\mathbf{n})]^2 d\mathbf{n} = \int \left[\left(C + C_{ij}n_in_j + C_{ijkl}n_in_jn_kn_l + \cdots\right) - f(\mathbf{n})\right]^2 d\mathbf{n} \rightarrow min. \quad 3$$

Where Er is the square of error and C, C_{ij}, C_{ijkl} ... are the coefficients of the polynomial approximation $F(\mathbf{n})$. The polynomial approximation was adopted for its simplicity and since it yields the approximated distribution in terms of linear expression of the fabric tensor of the first kind $N_{i_i i_2 \dots i_r}$. It is important to note that odd powers of **n** drops out of Equation 3 since $f(\mathbf{n})$ and so the approximation $F(\mathbf{n})$ are symmetric about the origin. Moreover, the coefficients are not uniquely determined since they are not linearly independent (i.e., $n_in_jn_kn_l$ contracts to n_in_j when $k = l$). However, Kanatani (1984) observed that if V_r is the vector space function on the unit sphere S^2 spanned by $n_{i_1}n_{i_2} \dots n_{i_r}$, then $V_0 \subset V_2 \subset V_4 \subset \cdots V_r$. Consequently, if the approximation is desired up to the r^{th} order, then $n_{i_1}n_{i_2} \dots n_{i_r}$ alone is sufficient as a basis. As a result, the r^{th} approximation of $f(\mathbf{n})$ can be expressed as:

$$f(\mathbf{n}) \sim \frac{1}{4\pi} F_{i_1 \mathrm{i}_1 \dots i_r} n_{i_1} n_{i_2} \dots n_{i_r} \quad 4$$

Where $F_{i_1 \mathrm{i}_1 \dots i_r}$ is the fabric tensor of the second kind of rank r, also known as fabric tensor. $F_{i_1 \mathrm{i}_1 \dots i_r}$ is determined by minimizing the square of error Er (i.e., $dEr/dF_{i_1 \dots i_r} = 0$) which gives:

$$F_{j_1 \ldots j_r} \frac{\int n_{j_1} \ldots n_{j_r} n_{i_1} \ldots n_{i_r} \, d\mathbf{n}}{4\pi} = N_{i_1 \ldots i_r} \qquad 5$$

Using the identity:

$$\frac{\int n_{i_1} n_{i_2} \ldots n_{\mathrm{i}_{2r}} \, d\mathbf{n}}{4\pi} = \frac{1}{2r+1} \delta_{(i_1 i_2} \delta_{i_3 i_4} \ldots \delta_{i_{2r-1} i_{2r})} \qquad 6$$

Then explicit expressions for the second and fourth order fabric tensors of the second kind can be expressed as (Kanatani 1984):

$$F_{ij} = \tfrac{15}{2} (N_{ij} - \tfrac{1}{5} \delta_{ij}) \qquad 7$$

$$F_{ijkl} = \tfrac{315}{8} (N_{ijkl} - \tfrac{2}{3} \delta_{(ij} N_{kl)} + \tfrac{1}{21} \delta_{(ij} \delta_{kl)}) \qquad 8$$

where δ is the Kronecker delta. For better understanding of the fundamental meaning of fabric tensors (i.e., first and second kind fabric tensors), tensors are visualized as 3D ellipsoidal glyphs (ellipsoidal representation surfaces) whose shape in a specific direction gives an immediate indication of the percentage of contacts in that direction. The formula of a point on representation surfaces can be expressed as:

$$S(\mathbf{n}) = \frac{1}{4\pi} E_{i_1 i_2 \ldots i_r} n_{i_1} n_{i_2} \ldots n_{i_r} \qquad 9$$

In which $E_{i_1 i_2 \ldots i_r}$ is the r^{th} ranked fabric tensor of the first kind ($N_{i_1 i_2 \ldots i_r}$) or the second kind ($F_{i_1 i_2 \ldots i_r}$). Surface representations of 2nd and 4th order fabric tensors of the first and second kind ($\mathbf{N2}, \mathbf{N4}, \mathbf{F2}$, and $\mathbf{F4}$) were plotted and discussed in the following chapter.

Fabric Evolution

2nd order fabric tensor of the 2nd kind ($\mathbf{F2}$) is a 3×3 symmetric matrix that describes the internal anisotropy of the material and is decomposable into deviatoric and isotropic components. The deviatoric component, which is hereafter referred to as $\mathbf{F}$, contributes to differences in material strength that are attributed to fabric-induced internal anisotropy. The main constituents of micro-mechanical interpretations of fabric are direction and magnitude, which can be incorporated into a macroscopic continuum mechanics description. Li and Dafalias (2011) introduced the second norm of fabric tensor $\mathbf{F}$ [$\mathrm{norm}(\mathbf{F}) = F \geq 0$] as a measure of the magnitude and the unit-norm deviatoric tensor-valued direction $\mathbf{n}_F$ of $\mathbf{F}$ to describe the direction of fabric:

$$\mathbf{F} = F\mathbf{n}_F, \qquad F = \sqrt{\mathbf{F}:\mathbf{F}}, \qquad \mathbf{n}_F:\mathbf{n}_F = 1, \qquad \mathrm{tr}(\mathbf{n}_F) = 0 \qquad 10$$

Where the symbol : implies the trace (tr) of the product of two adjacent tensors and in geometrical terms can be thought as being their scaler product [i.e., $\mathbf{A}:\mathbf{B} = \mathrm{tr}(\mathbf{AB}) = A_{ij}B_{ji}$]. To incorporate the resistance of fabric against loading, Li and Dafalias (2011) introduced the unit-norm deviatoric tensor-valued loading direction $\mathbf{n}$, where $\mathbf{n}:\mathbf{n} = 1$ and $\mathrm{tr}(\mathbf{n}) = 0$. For example, in triaxial monotonic loading $\mathbf{n}$ coincides with the direction of the applied deviatoric stress. Subsequently, the fabric anisotropic variable A, referred to as FAV A, is defined as:

$$\text{FAV } A = \mathbf{F}:\mathbf{n} = F\mathbf{n}_F:\mathbf{n} = FN \qquad 11$$

F is normalized such that at critical state $F_c = 1$, resulting in FAV A to approach $A_c = 1$ at critical state. Normalized FAV A accounts for both magnitude of fabric and its orientation relative to loading direction. Normalized FAV A was adopted in this thesis to experimentally characterize fabric evolution.

CHAPTER THREE: RESULTS AND DISCUSSION

Fabric and Fabric Evolution

Fabric for F35_D_400 experiment is fully presented in Figures 3-5 including 3D spherical histograms and representation surfaces of the 2nd and 4th order moment and fabric tensors at ε_1 associated with SMT scans (Figure 1). It can be observed from Figures 3-5 that F35_D_400 experiment exhibited the highest degree of internal isotropy at the initial configuration (i.e., $\varepsilon_1 = 0\%$) with nearly no preferential orientation of contact normals. In other words, representation surfaces of moment and fabric tensors were closest to spherical shapes at $\varepsilon_1 = 0\%$. Particles were expected to lay along their long axes as they were deposited by gravity with an initial preferential orientation of contact normals toward the vertical (i.e., principal stress direction of gravity). Nevertheless, the effect of the applied confining pressure (σ_3) cannot be ignored as the initial SMT scan was acquired after confinement. σ_3 of $400\ kPa$ was applied equally at all boundaries since a cylindrical specimen under constant σ_3 was tested. Accordingly, the confining pressure counter-balanced the deposition preferential orientation of contact normals and caused a more isotropic spherical shape of representation surfaces for both fabric and moment tensors. As ε_1 was increased, particles were jammed into a network of mutual compressive forces that were mostly aligned in the direction of the global applied compression load (i.e., vertical direction). Therefore, representation surfaces of moment and fabric tensors in Figures 3-5 generally evolved from spherical isotropic shapes to ellipsoidal glyphs with preferential orientation pointing toward the vertical resulting in a higher degree of internal anisotropy.

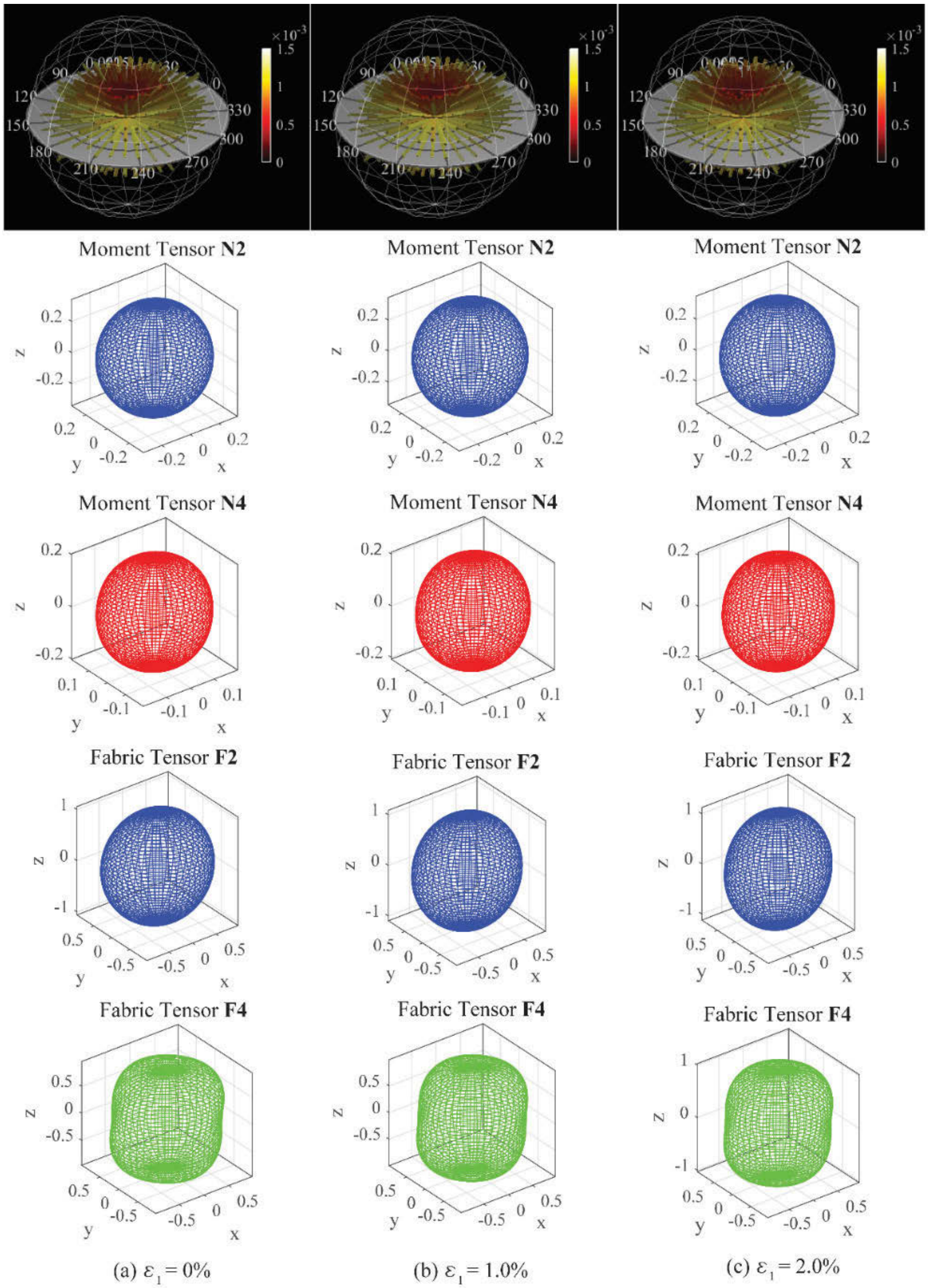

Figure 3. 3D spherical histogram with **N2**, **N4**, **F2**, and **F4** representation surfaces of global contact unit normal vectors for F35_D_400 experiment at (a) $\varepsilon_1 = 0\%$; (b) $\varepsilon_1 = 1.0\%$; and (c) $\varepsilon_1 = 2.0\%$.

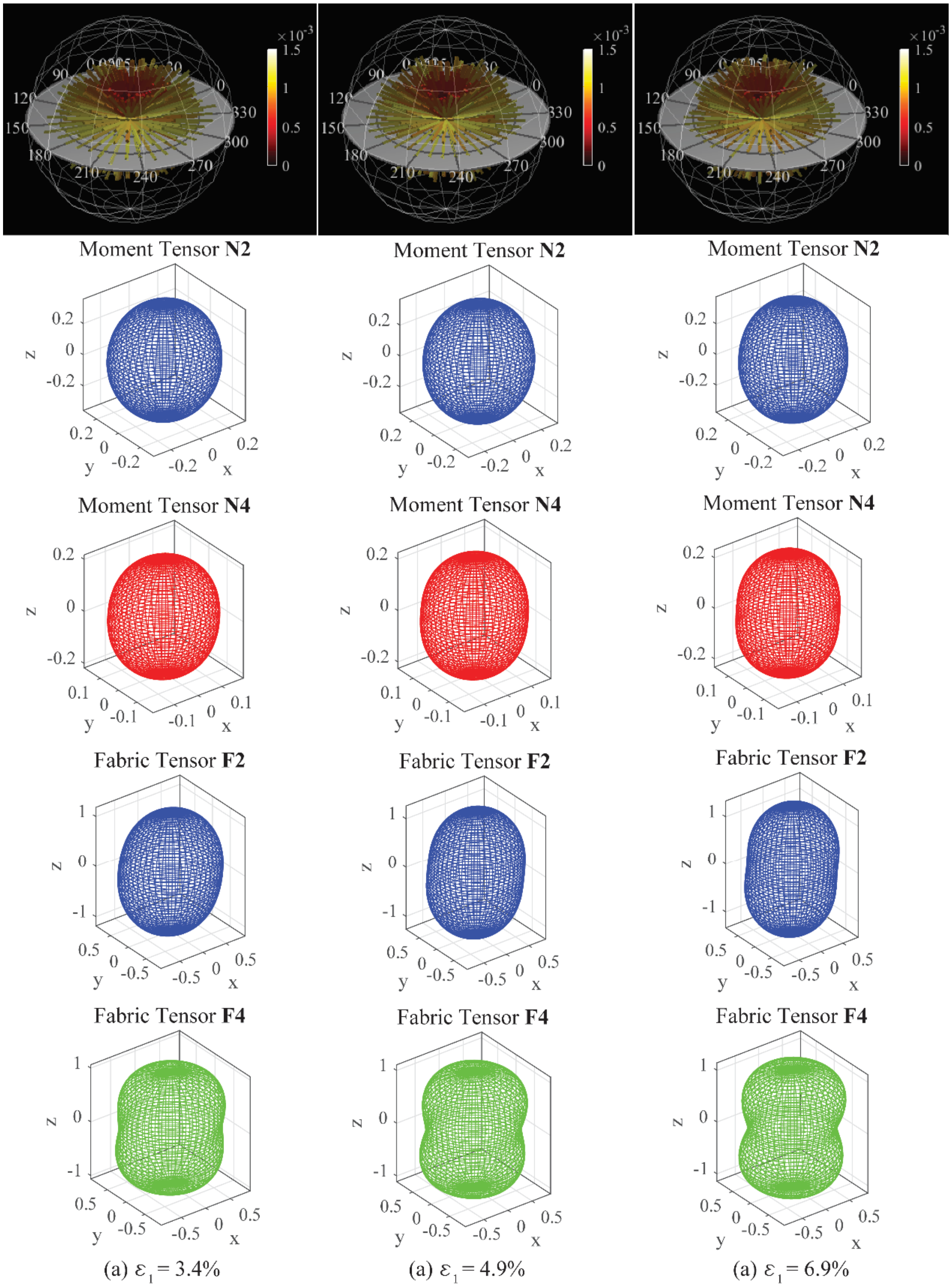

Figure 4. 3D spherical histogram with **N2**, **N4**, **F2**, and **F4** representation surfaces of global contact unit normal vectors for F35_D_400 experiment at (a) $\varepsilon_1 = 3.4\%$; (b) $\varepsilon_1 = 4.9\%$; and (a) $\varepsilon_1 = 6.9\%$.

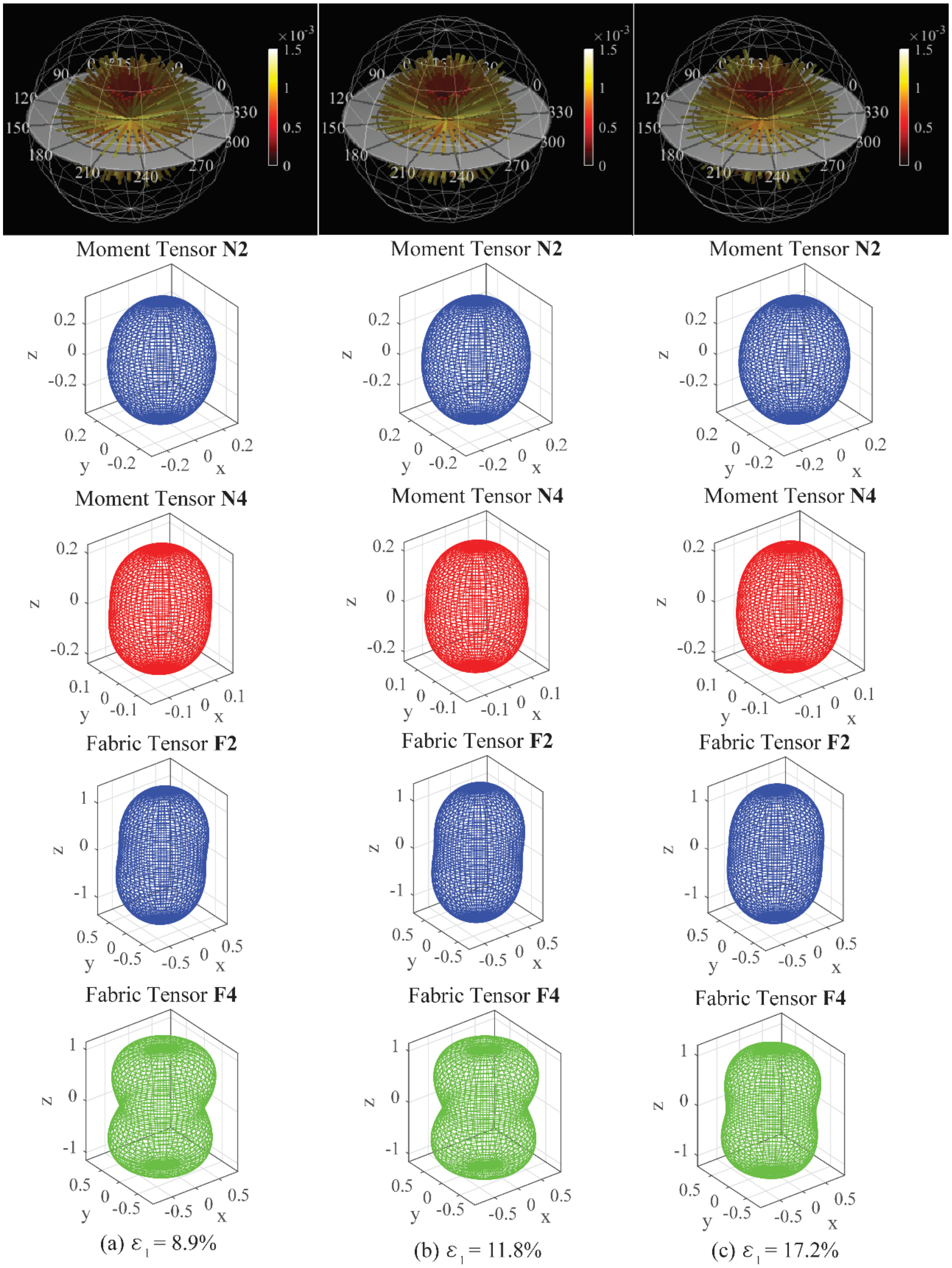

Figure 5. 3D spherical histogram with **N2**, **N4**, **F2**, and **F4** representation surfaces of global contact unit normal vectors for F35_D_400 experiment at (a) $\varepsilon_1 = 8.9\%$; (b) $\varepsilon_1 = 11.8\%$; and (a) $\varepsilon_1 = 17.2\%$.

Representation surfaces displayed in Figures 3-5 includes two kinds of tensors (i.e., moment versus fabric). It can be inferred from Figures 3-5 that the introduction of the distribution density term in the fabric tensor led to a better interpretation of the actual experimental data. In other words, **F2** and **F4** representation surfaces better match the 3D spherical histograms than **N2** and **N4**, respectively. Furthermore, a higher degree of estimate yielded a higher degree of fitting between experimental data and calculated tensors (i.e., 4^{th} order estimates of **N4** and **F4** better match the 3D spherical histograms than 2^{nd} order estimates of **N2** and **F2**, respectively). Note that the 3D spherical histograms represent the actual distribution of contact normals; however, the complexity of the isometric view of 3D spherical histograms made it difficult to visualize differences between different directional data. Therefore, the 4^{th} order fabric tensor **F4** was considered for further fabric assessment and comparison. To better illustrate the match between **F4** fabric tensor and actual experimental data, horizontal (X-Y) and vertical (Y-Z and X-Z) views of **F4** representation surface and 3D spherical histograms for F35_D_400 experiment are depicted in Figures 6-8 at $\varepsilon_1 = 1\%$, 4.9% and 11.8%, respectively. Toward initial loading stage (Figure 6), the horizontal and vertical views (i.e., X-Y, X-Z, and Y-Z) exhibited the highest degree of isotropy (i.e., 2D projections of **F4** representation surfaces were closest to a circular shape). Again, this emphasized on the higher degree of internal isotropy that was observed at initial configuration (i.e., $\varepsilon_1 = 0\%$). A minor distortion can be still noticed in the Y-Z view in Figure 6(c) which can be attributed to imperfections in specimen preparation. As compression progressed (Figures 7-8), the X-Y view of the **F4** fabric tensor maintained its isotropic circular shape until the onset of a single well-defined shear band near the final loading stages between 8.9% and 11.8% ε_1 [Figure 2(g) and (h), respectively]. Shear band effect can be clearly noticed in Figure 8(a) in which the X-Y view lost its vertical alignment relative to the X-Y views in Figures 6(a) and 7(a). Referring to the vertical views, axial compression induced a preferential orientation of contact normals toward loading direction. Thus, the X-Z and Y-Z views in Figure 6 distorted from an isotopic circular shape into lemniscate shapes in which expansion occurred towards the vertical (i.e., more contact normals close to the vertical direction) and necking toward the center (i.e., less contact normals pointing toward the horizontal plane) as illustrated in Figures 7-8; accordingly, the internal anisotropy of the granular assembly increased. Note that Kanatani (1984) reported similar 2D lemniscate shapes for 2D directional data of contact normals for compressed assembly of oval rods (i.e., 2D granular material).

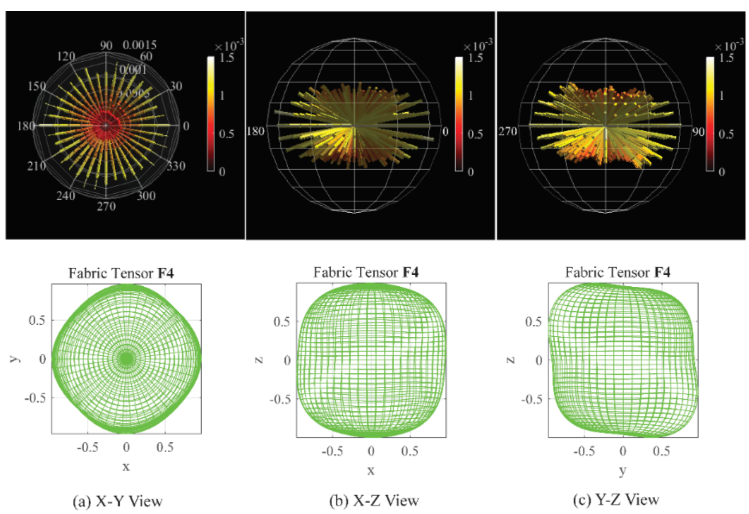

Figure 6. (a) X-Y, (b) X-Z, and (c) Y-Z views for the 3D spherical histogram and **F4** representation surface of global contact unit normal vectors for the F35_D_400 experiment at ε_1=1.0%.

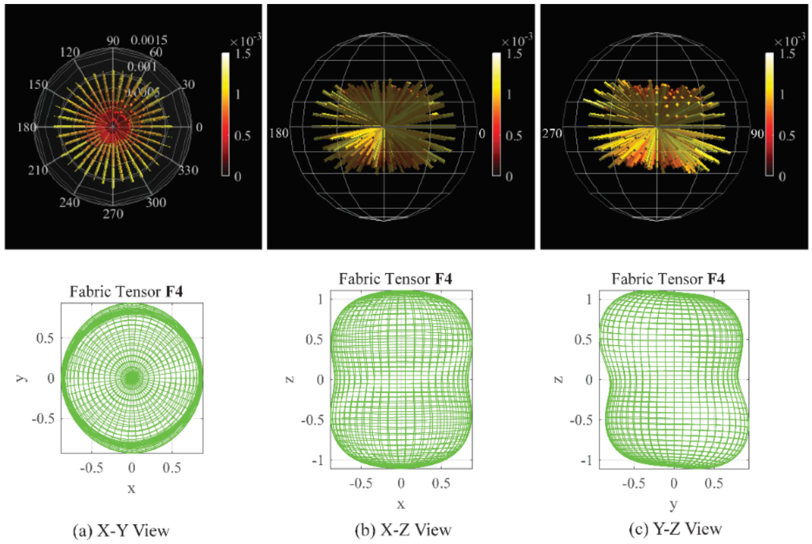

Figure 7. (a) X-Y, (b) X-Z, and (c) Y-Z views for the 3D spherical histogram and **F4** representation surface of global contact unit normal vectors for the F35_D_400 experiment at $\varepsilon_1 = 4.9\%$.

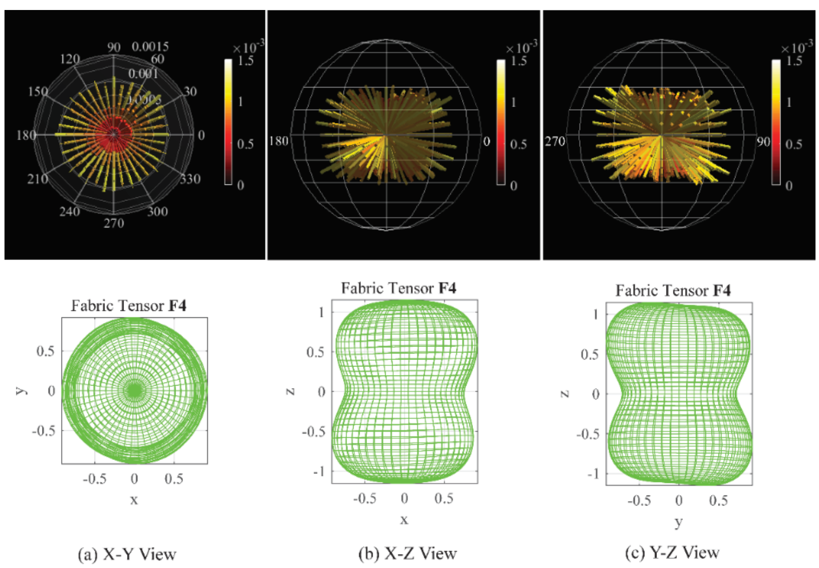

Figure 8. (a) X-Y, (b) X-Z, and (c) Y-Z views for the 3D spherical histogram and **F4** representation surface of global contact unit normal vectors for the F35_D_400 experiment at $\varepsilon_1 = 11.8\%$.

FAV A was calculated for each SMT scan of the F35_D_400 experiment, taking into account the unit-norm deviatoric tensor-valued loading direction **n** for conventional triaxial compression. As a common practice influenced by the theoretical evolution of FAV A in Li and Dafalias (2011), the maximum FAV A for each experiment was normalized to unity ($A_c = A_{max} = 1$). Normalizing FAV A scales initial fabric and does not affect fabric evolution. Evolution of FAV A and principal stress ratio (PSR = $\sigma 1/\sigma 3$) versus ε_1 for the F35_D_400 experiment is depicted in Figure 9. Initially, FAV A for F35_D_400 experiment emerged from 0.62 and steadily increased until $\varepsilon_1 = 8.9\%$, where it began to approach unity. Correspondingly, PSR commenced from unity and steadily increased until it peaked and approached critical state shortly after $\varepsilon_1 = 8.9\%$. Furthermore, it can be observed from Figure 5 that the specimen approached a steady fabric around $\varepsilon_1 = 8.9\%$ (i.e., similar shape of representation surfaces and 3D spherical histograms for ε_1 equal to 8.9% and 11.8%). The concurrence of critical state condition and approaching a steady fabric supports the Anisotropic Critical State theory (ACST) which suggests that a steady fabric must be satisfied in parallel with a constant volume and deviatoric stress for the critical state to occur (Dafalias 2016). Nonetheless, representation surfaces of fabric tensors were observed to change at $\varepsilon_1 = 17.2\%$ (i.e., final scan) from the steady fabric attained at the critical state. This was attributed to the excessive shearing (i.e., deformation) along the single well-defined shear band as depicted in Figure 2(i). This can also be related to the drop in FAV A value at $\varepsilon_1 = 17.2\%$ in Figure 9.

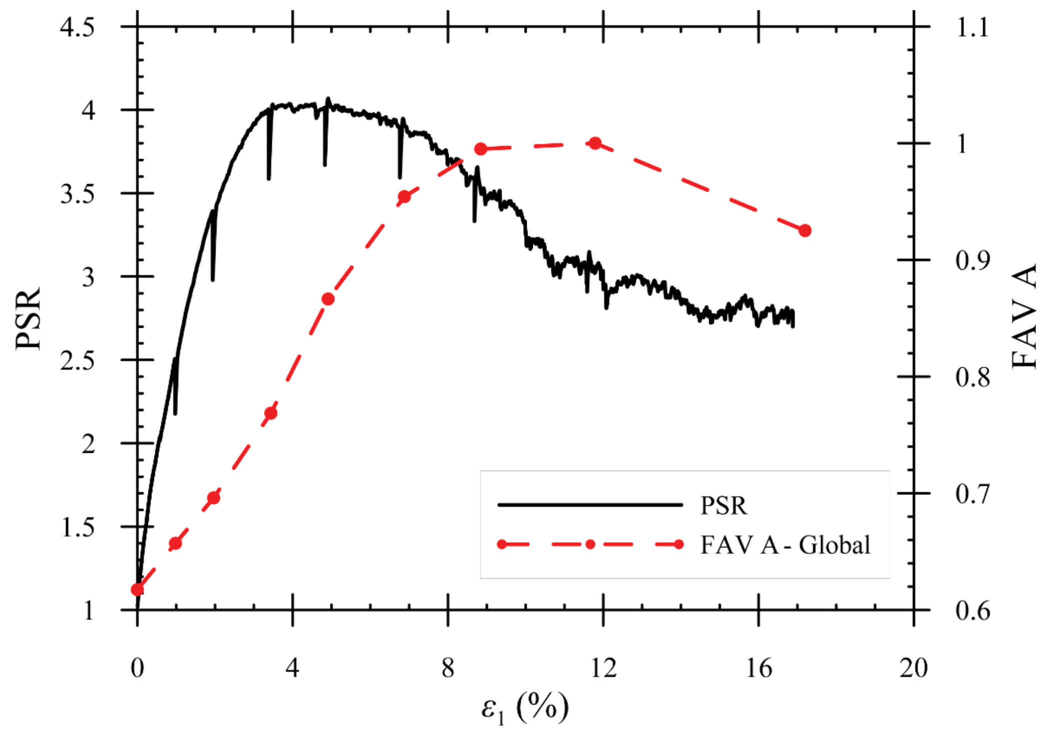

Figure 9. Evolution of PSR and FAV A versus ε_1 for F35_D_400 experiment.

Overall, a similar general behavior was observed for the other nine experiments (i.e., 3D spherical histograms evolved toward the vertical direction, representation surfaces distorted from isotropic close to spherical shapes into 3D lemniscate shapes, and normalized FAV A approached unity at the critical state) with certain differences to be discussed later. Fabric of the other nine experiments is concisely summarized in Figures 10-18 including 3D spherical histograms and **F4** representation surfaces of initial and final loading stages. In addition, the evolution of FAV A including all loading stages is also displayed in Figures 10-18 for each experiment.

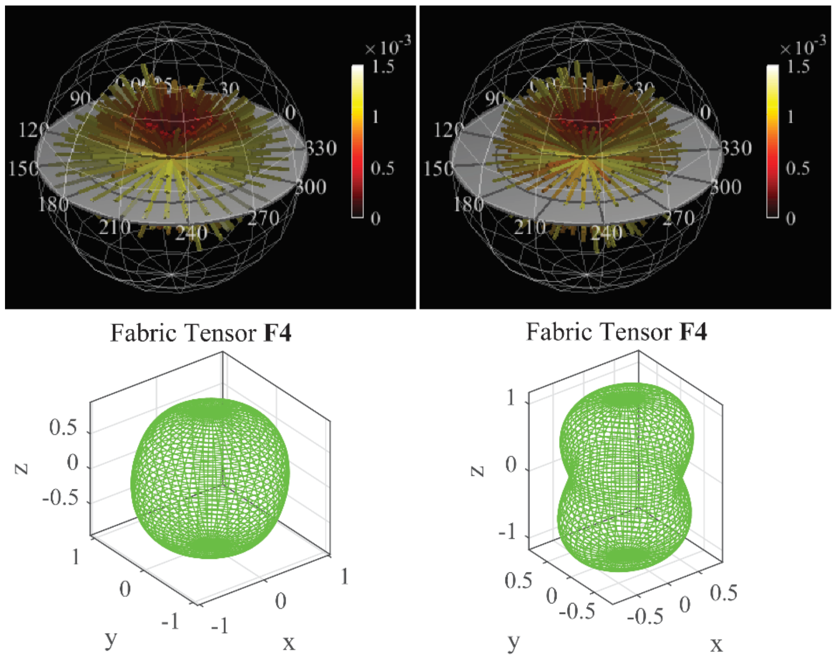

(a) Inital fabric (b) Final fabric

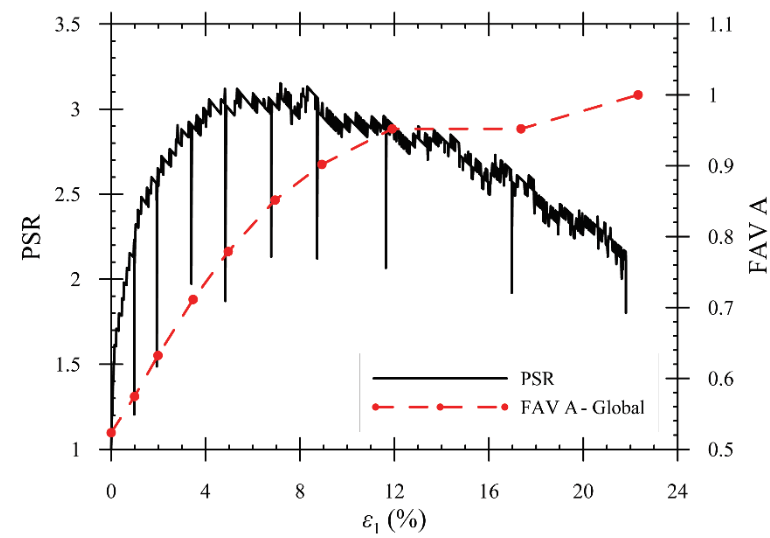

(c) Fabric evolution

Figure 10. 3D spherical histogram with **F4** representation surface of global contact unit normal vectors at (a) initial and (b) last loading stage for F35_D_15 experiment and (c) the evolution of PSR and global FAV A versus ε_1.

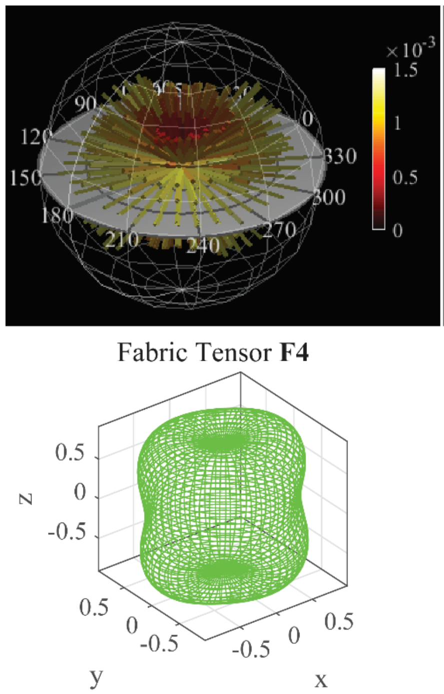

(a) Inital fabric

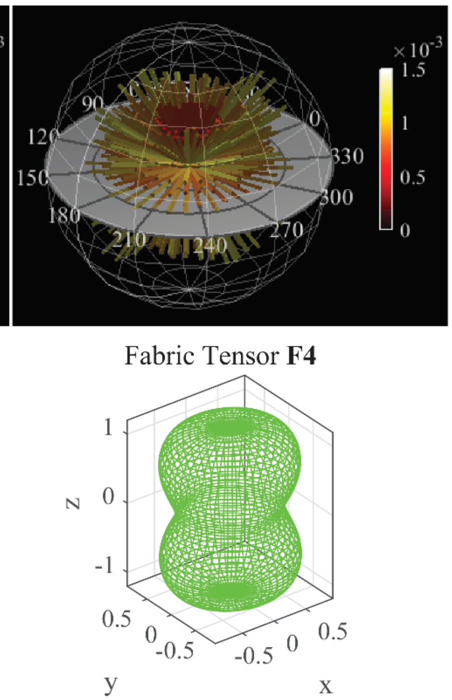

(b) Final fabric

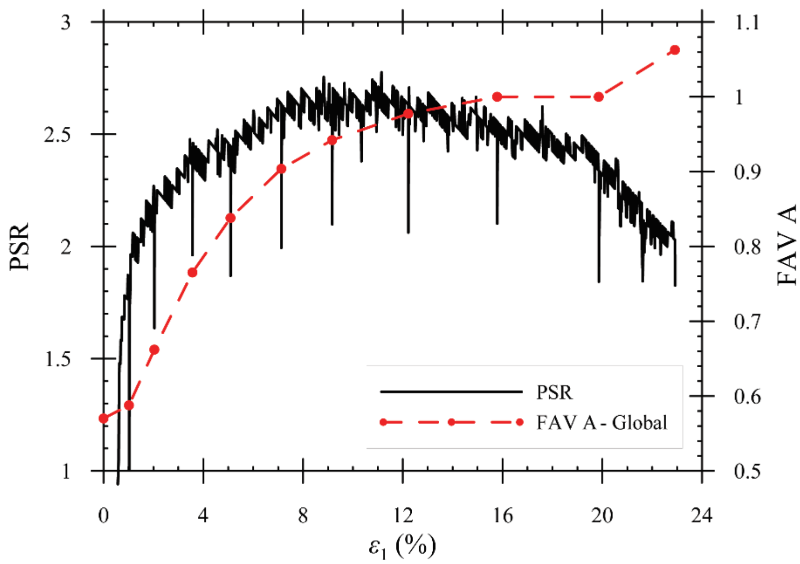

(c) Fabric evolution

Figure 11. 3D spherical histogram with **F4** representation surface of global contact unit normal vectors at (a) initial and (b) last loading stage for F35_MD_15 experiment and (c) the evolution of PSR and global FAV A versus ε_1.

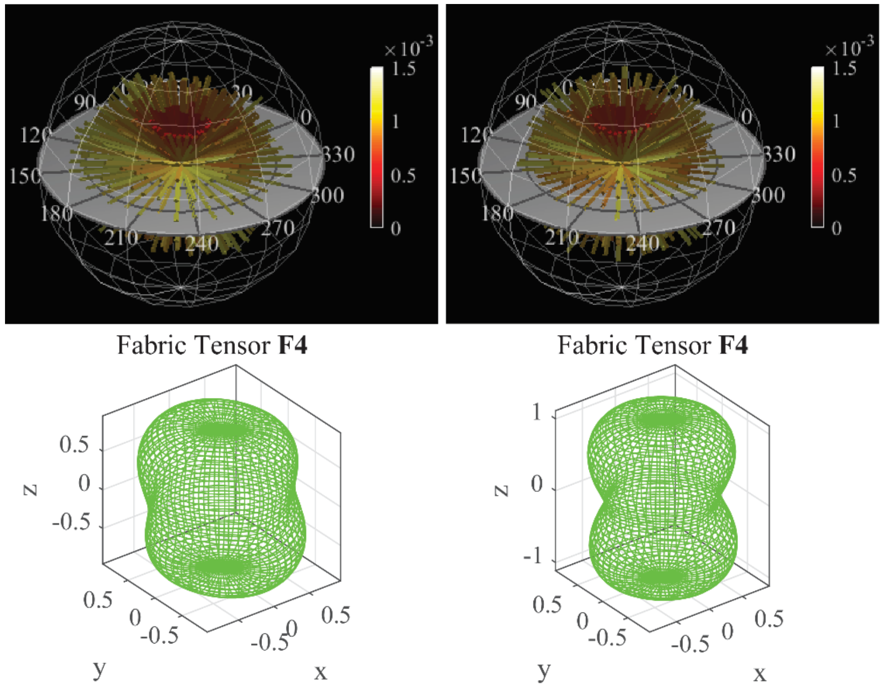

(a) Inital fabric

(b) Final fabric

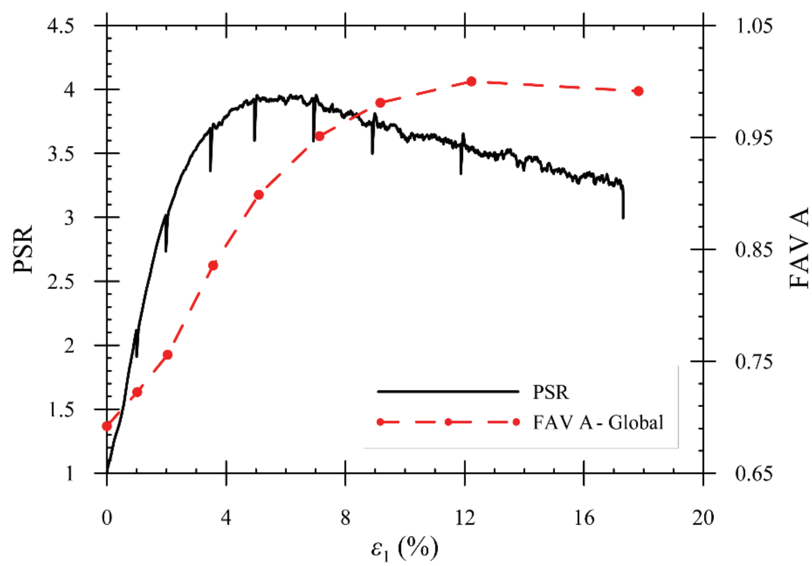

(c) Fabric evolution

Figure 12. 3D spherical histogram with **F4** representation surface of global contact unit normal vectors at (a) initial and (b) last loading stage for DG_D_400 experiment and (c) the evolution of PSR and global FAV A versus ε_1.

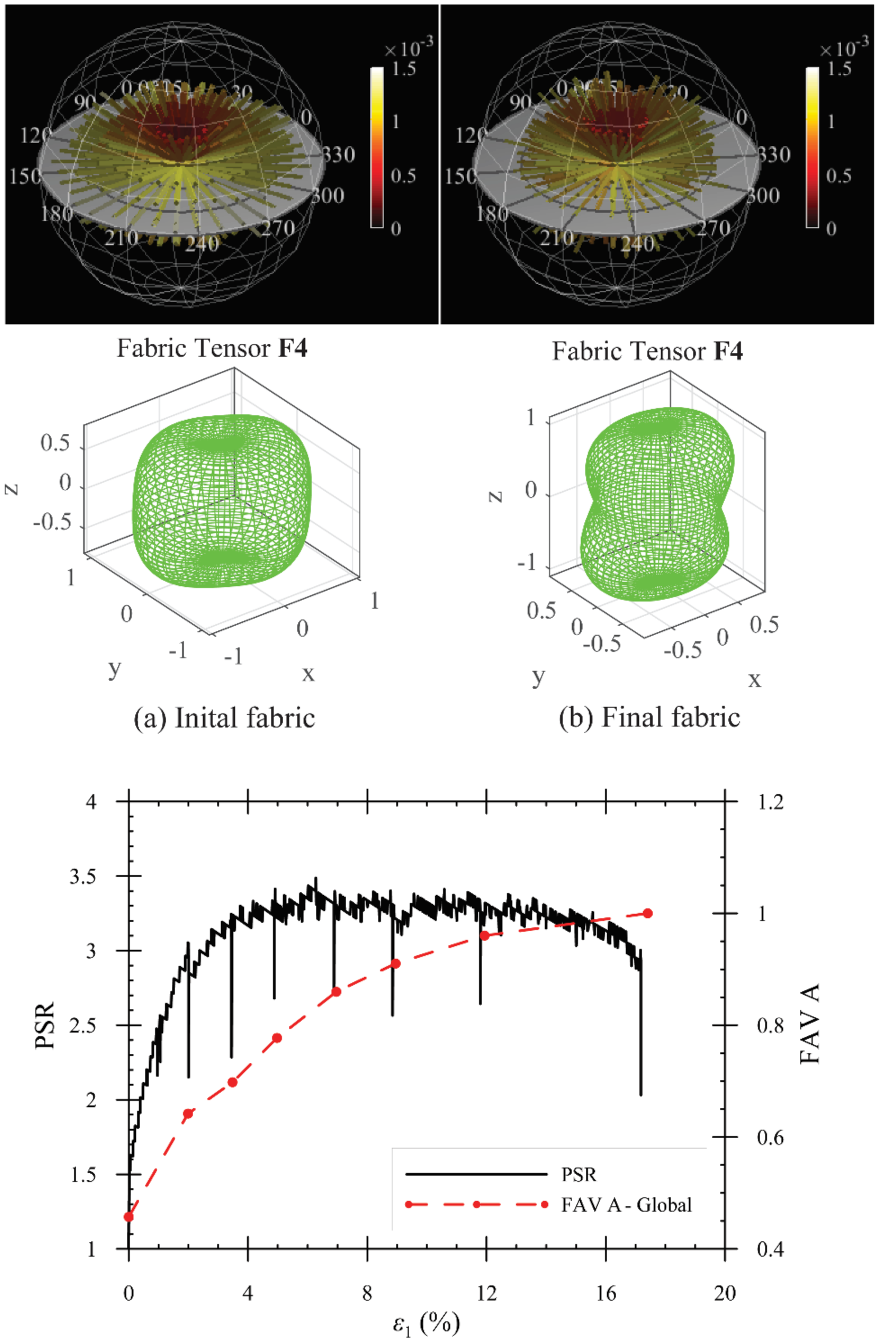

(c) Fabric evolution

Figure 13. 3D spherical histogram with **F4** representation surface of global contact unit normal vectors at (a) initial and (b) last loading stage for DG_D_15 experiment and (c) the evolution of PSR and global FAV A versus ε_1.

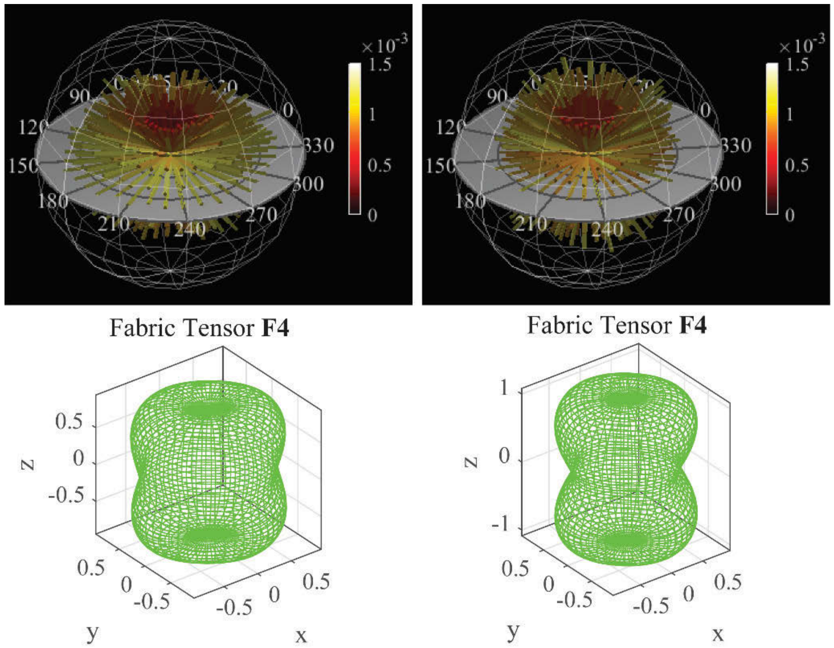

(a) Inital fabric (b) Final fabric

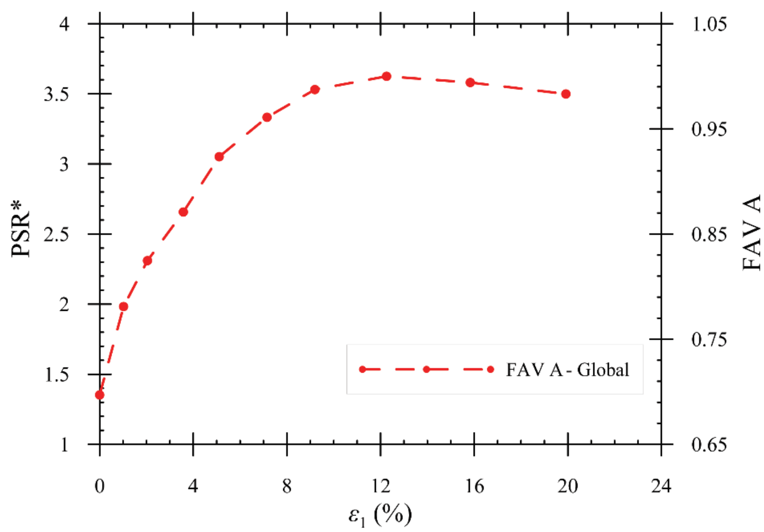

(c) Fabric evolution

Figure 14. 3D spherical histogram with **F4** representation surface of global contact unit normal vectors at (a) initial and (b) last loading stage for DG_MD_15 experiment and (c) the evolution of PSR and global FAV A versus ε_1 (*Load cell was not recording data during this experiment).

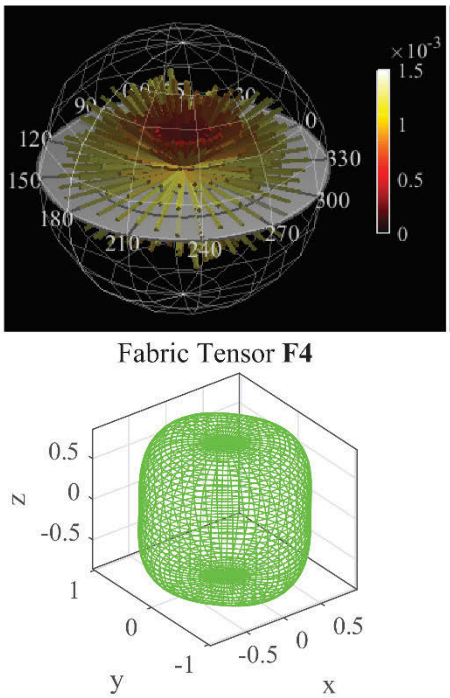

(a) Inital fabric

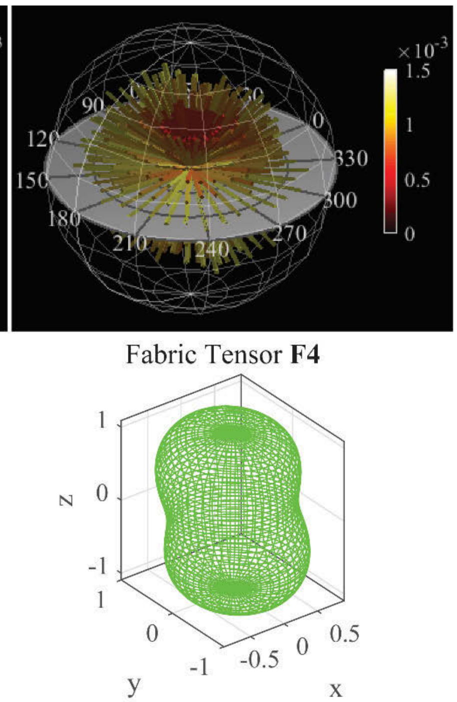

(b) Final fabric

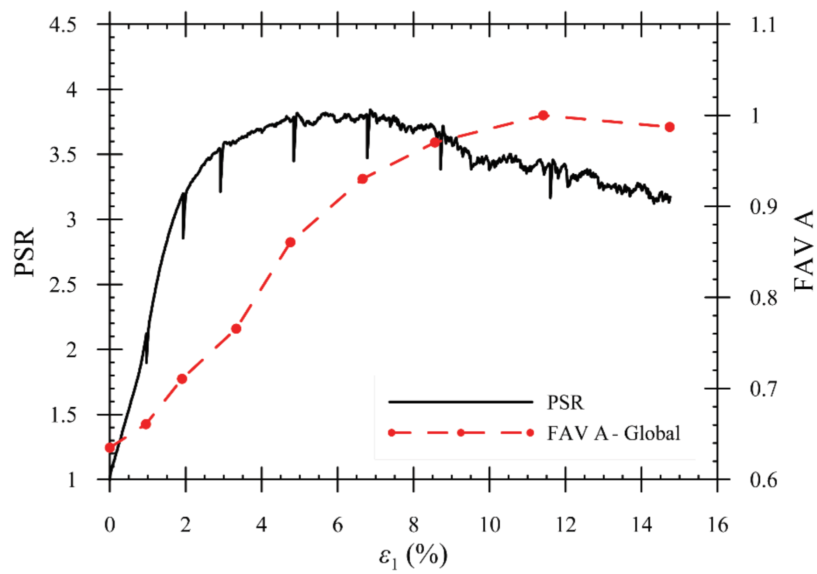

(c) Fabric evolution

Figure 15. 3D spherical histogram with **F4** representation surface of global contact unit normal vectors at (a) initial and (b) last loading stage for GS40_D_400 experiment and (c) the evolution of PSR and global FAV A versus ε_1.

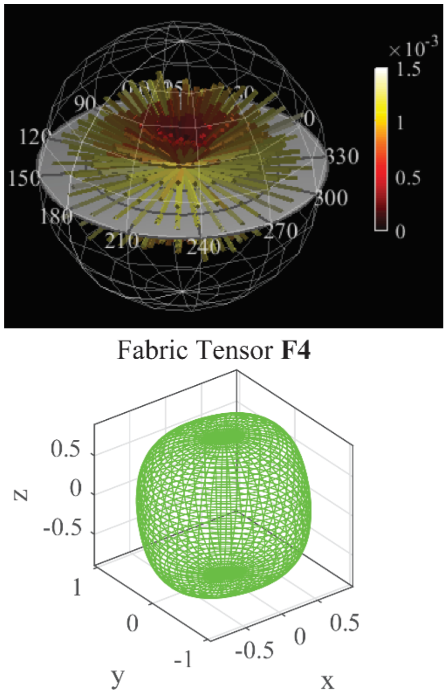

(a) Inital fabric

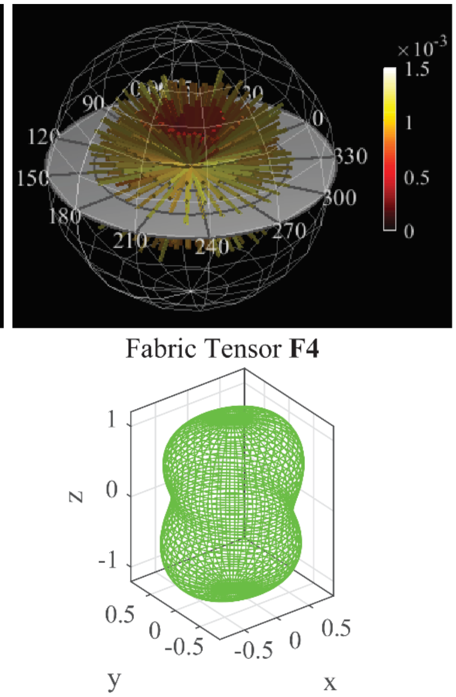

(b) Final fabric

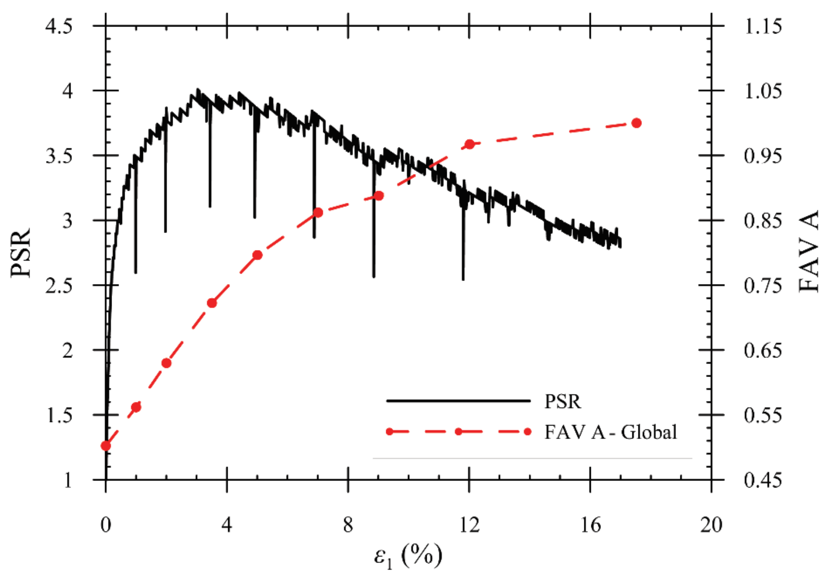

(c) Fabric evolution

Figure 16. 3D spherical histogram with **F4** representation surface of global contact unit normal vectors at (a) initial and (b) last loading stage for GS40_D_15 experiment and (c) the evolution of PSR and global FAV A versus ε_1.

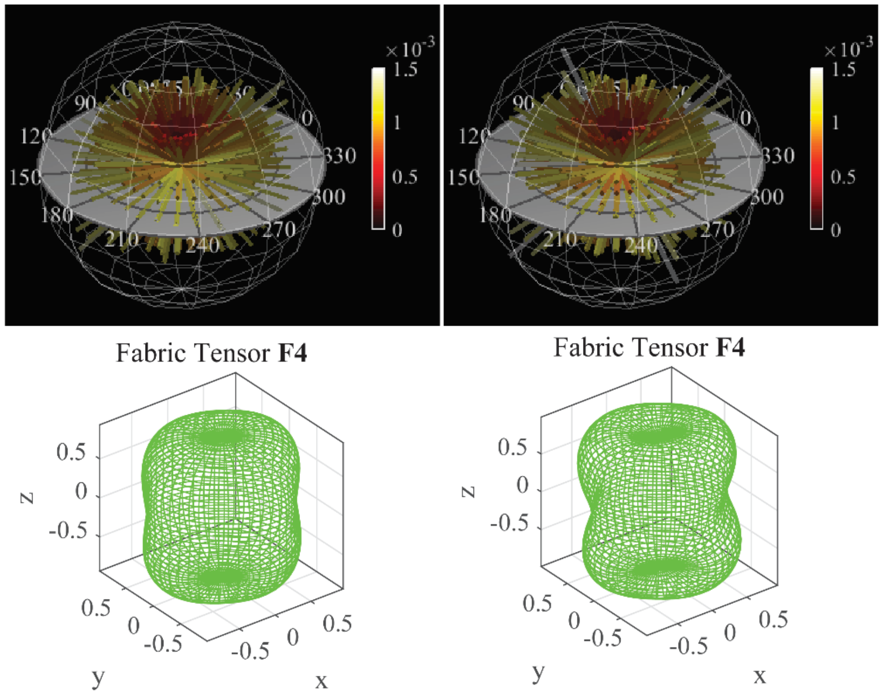

(a) Initial fabric

(b) Final fabric

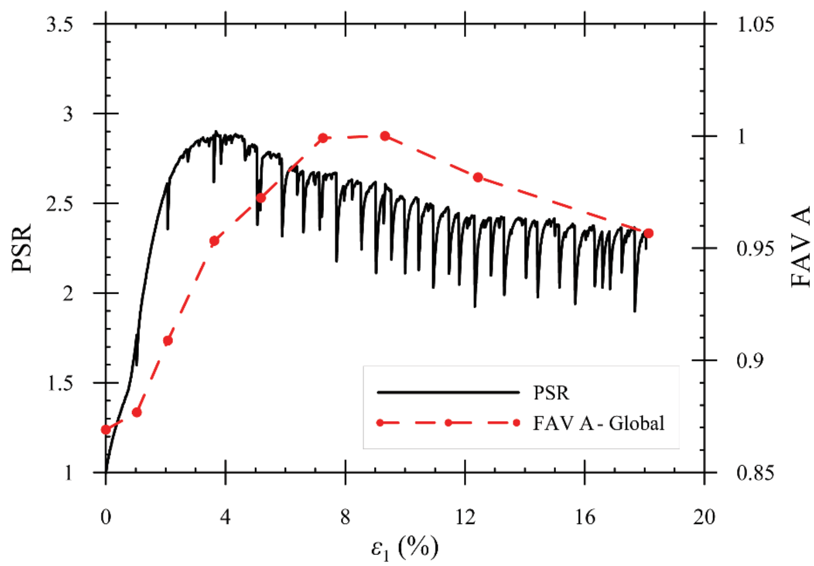

(c) Fabric evolution

Figure 17. 3D spherical histogram with **F4** representation surface of global contact unit normal vectors at (a) initial and (b) last loading stage for GB_D_400 experiment and (c) the evolution of PSR and global FAV A vresus ε_1.

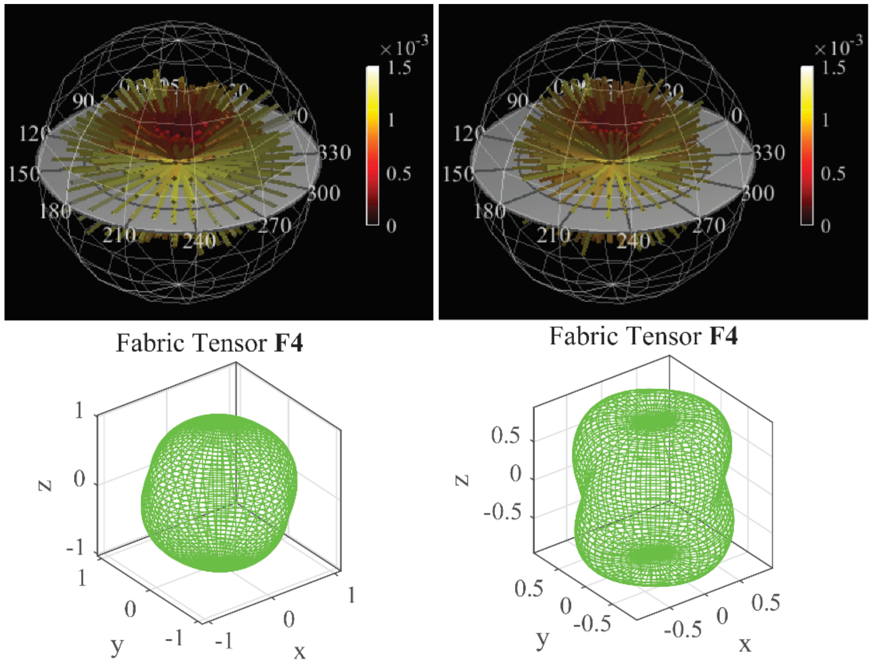

(a) Inital fabric

(b) Final fabric

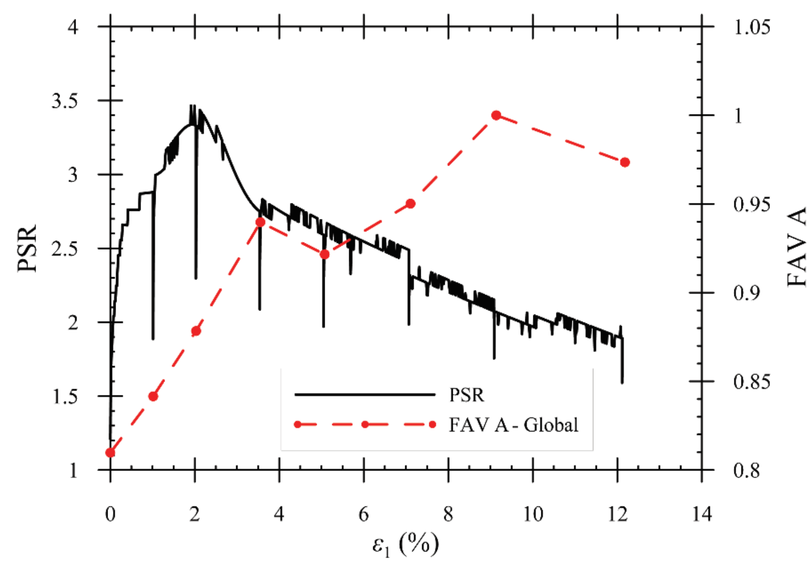

(c) Fabric evolution

Figure 18. 3D spherical histogram with **F4** representation surface of global contact unit normal vectors at (a) initial and (b) last loading stage for GB_D_15 experiment and (c) the evolution of PSR and global FAV A vresus ε_1.

Influence of Specimen Density and Applied Confining Pressure

It is well-known that specimen density, confining pressure, and particle-level morphology significantly influence failure modes of sand specimens under conventional triaxial compression (Alshibli et al. 2003; Alshibli et al. 2016; Desrues and Andò 2015; Desrues et al. 1996). Processed SMT scans showed that dense specimens tested under high σ_3 failed via a single well-defined shear band while bulging occurred in looser state specimens tested under low σ_3. Bulging was investigated in Amirrahmat et al. (2017) to be external manifestation of intense internal shearing through multiple micro shear bands formed in opposite directions. Low confinement (i.e., $\sigma_3 = 15\ kPa$) allowed a higher degree of freedom for the specimen to expand laterally and develop multiple shearing planes (i.e., multi-micro shear bands). Conversely, high confinement (i.e., $\sigma_3 = 400\ kPa$) inhibited lateral expansion; therefore, localization of shear ultimately grew in the single evolved shear plane rather than creating multiple shear planes at the critical state. A detailed study that investigates failure modes and internal failure pattern for the conducted experiments by means of particle kinematics and visual inspection can be found in Alshibli et al. (2016) and Amirrahmat et al. (2017) as it is considered beyond the scope of this study. To evaluate the influence of specimen density and σ_3 on fabric evolution of granular materials, experiments conducted on the same material (i.e., same morphology) were examined and compared while holding a variable constant (i.e., initial density state or σ_3) and changing the other. Starting with the effect of density, medium dense specimens tested at $\sigma_3 = 15\ kPa$ were compared with dense specimens tested at the same σ_3 (i.e., specimens F35_MD_15 versus F35_D_15, and DG_MD_15 versus DG_D_15) as illustrated in Figure 19. It can be observed from Figure 19(a) that specimens with a higher initial density (i.e., F35_D_15 and DG_D_15 specimens) exhibited a higher degree of internal isotropy than medium dense specimens (i.e., F35_MD_15 and DG_MD_15) at the initial configuration (i.e., $\varepsilon_1 = 0\%$). In other words, the **F4** representation surfaces of F35_D_15 and DG_D_15, depicted in Figure 19(a), were closer to spherical shapes when compared with F35_MD_15 and DG_MD_15, respectively. This observation can directly be related to density effect on packing of particles. A higher density state led to a higher degree of packing which generated more contacts that were more likely to be distributed randomly resulting in a higher degree of internal isotropy. One the other hand, looser density state specimens contained less particles and contacts; hence, the preferential direction of contact normals toward the vertical axis due to deposition effects can still be observed in **F4** representation surfaces of medium dense specimens. This can explain the expansion of **F4** representation surfaces toward the vertical and contraction toward the horizontal plane for medium dense specimens in Figure 19(a). The influence of σ_3 was investigated by comparing fabric of dense specimens tested at $\sigma_3 = 400\ kPa$ with dense specimens tested at $\sigma_3 = 15\ kPa$ as illustrated in Figure 20. It can be observed from Figure 20(a) that specimens tested at $\sigma_3 = 15\ kPa$ initially exhibited a more isotropic distribution of contact normals than specimens tested at $\sigma_3 = 400\ kPa$. The influence of σ_3 on initial fabric can be linked to stress level effect on the distribution of inter-particle contact forces. The low σ_3 (i.e., $15\ kPa$ confinement) imposed less distortion on the ideal isotropic distribution of contact normal vectors than a higher σ_3 (i.e., $\sigma_3 = 400\ kPa$). Accordingly, the initial **F4** representation surfaces of F35_D_15, DG_D_15, GS40_D_15, and

GB_D_15, shown in Figure 20(a), were closer to spherical shapes when compared to F35_D_400, DG_D_400, GS40_D_400, and GB_D_400, respectively.

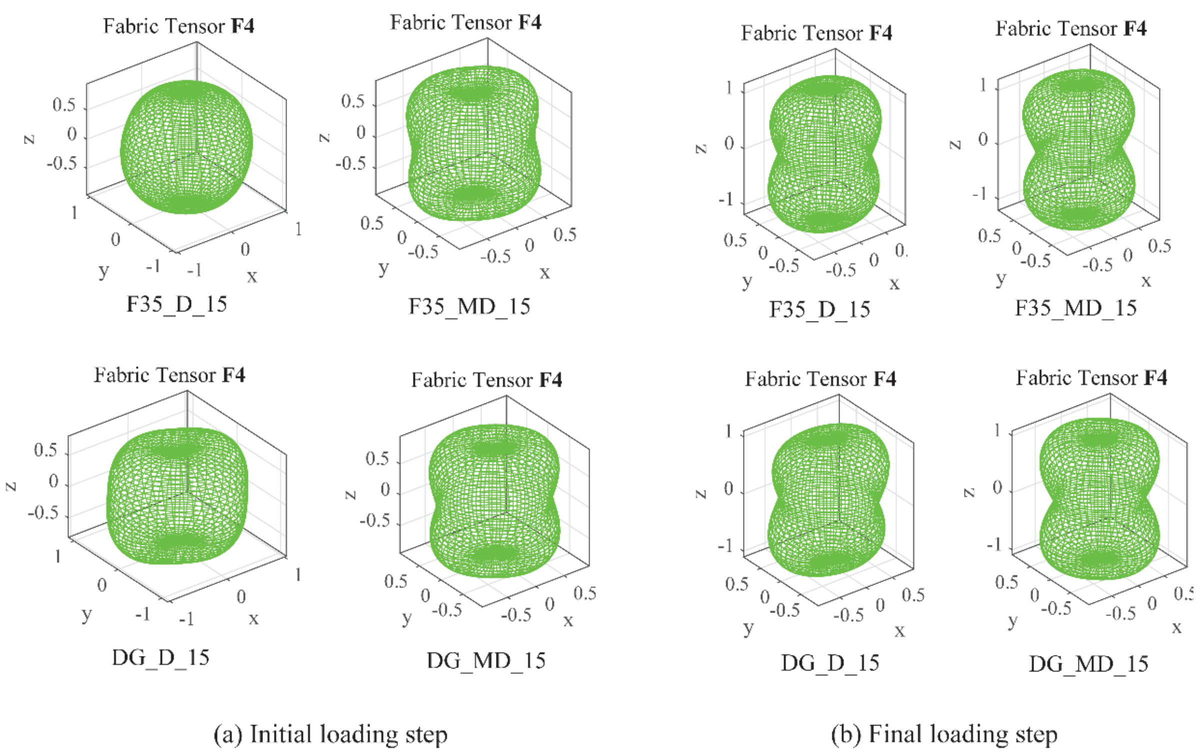

Figure 19. Comparison between **F4** representation surfaces of global contact unit normal vectors of dense 15 kPa versus medium dense 15 kPa experiments at (a) initial and (b) last loading stage.

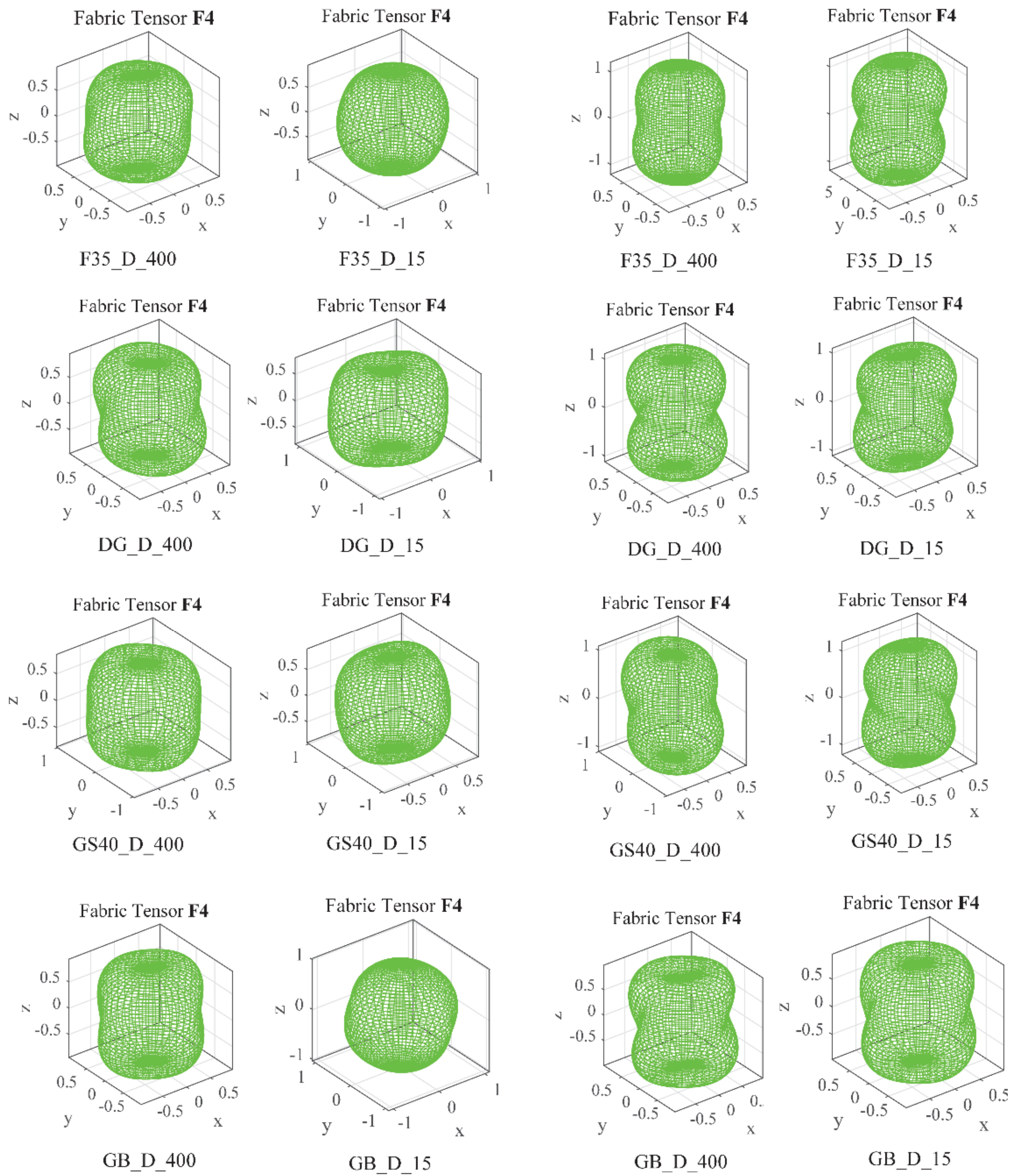

(a) Initial loading step (b) Final loading step

Figure 20. Comparison between **F4** representation surfaces of global contact unit normal vectors of dense 400 kPa versus desne 15 kPa experiments at (a) initial and (b) last loading stage.

Referring to fabric at final configuration (i.e., last loading stage), **F4** representation surfaces exhibited similar general shapes (i.e., 3D lemniscate shape) for all experiments as depicted in Figures 19-20. However, specimens that failed via a single well-defined shear band (F35_D_400, GS40_D_400, and GB_D_400 experiments) showed vertical misalignment in the **F4** representation surfaces toward final loading stages. Conversely, a higher degree of vertical alignment was noticed near final **F4** representation surfaces for experiments failed due to bulging. To further investigate the effect of single well-defined shear band failure on fabric, vertical views visualizing the single shear band formed in F35_D_400 experiment versus bulging developed in F35_D_15 and F35_MD_15 experiments were depicted in Figure 21 side-by-side with corresponding views in **F4** representation surfaces. SMT scans in Figure 21 clearly show that the development of a single shear band created a sliding wedge within the specimen. As sliding proceeded, particles were sheared in the direction of sliding which caused more contact to evolve in that direction. This can explain vertical misalignment in **F4** representation surfaces toward the distinct shear band direction in Figure 21(a). On the other hand, specimens failed due to bulging were internally visualized in Amirrahmat et al. (2017) by means of particle kinematics in which shear localization was observed to occur via multi-micro shear bands developed in oposite directions.; therefore, the vertical misalignment in **F4** representation surfaces did not exist. In conclusion, the vertical alignment of **F4** representation surfaces near the last loading stage was attributed to the type of failure mode (i.e., single well-defined shear banding versus bulging) which was significantly influenced by initial density state and confining pressure.

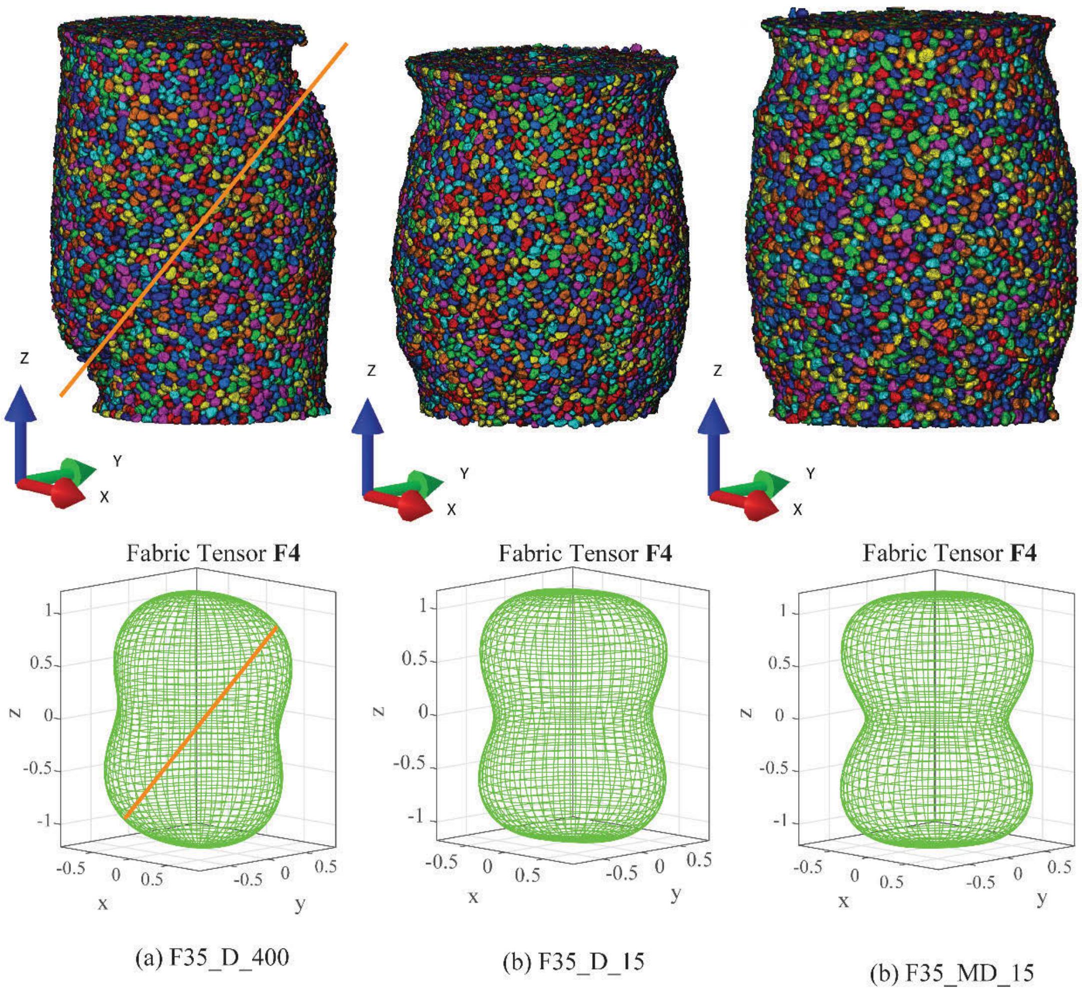

Figure 21. Demonstration of the influence of a single well-defined shear band on **F4** representation surfaces for (a) F35_D_400 (b) GS40_D_400 and (c) GB_D_400.

A similar approach was adopted to investigate the influence of specimen density and σ_3 on fabric evolution (i.e., changing one parameter while holding the other constant). Figure 22 presents the evolution of FAV *A* for F35_D_15 versus F35_MD_15 and DG_D_15 versus DG_MD_15 to evaluate the effect of specimen density on fabric evolution which shows that medium dense specimens exhibited higher FAV *A* values than dense specimens (i.e., a higher degree of fabric anisotropy). On the other hand, Figure 23 illustrates the evolution of FAV A for F35_D_15 versus F35_D_400, DG_D_15 versus DG_D_400, GS40_D_15 versus GS40_D_400, and GB_D_15 versus GB_D_400 experiments to evaluate the effect of σ_3 on fabric evolution. It can be noticed from Figure 23 that the $400\ kPa$ experiments exhibited higher FAV A values than experiments tested at $15\ kPa$ confinement which indicated a higher degree of fabric anisotropy. Both observations again advocated the profound influence of density and σ_3 on initial fabric (i.e., lower initial density and higher σ_3 results in higher degree of fabric-induced internal anisotropy). Furthermore, Figures 22-23 shows that FAV A evolved approximately in a similar slope regardless of specimen initial density and σ_3.

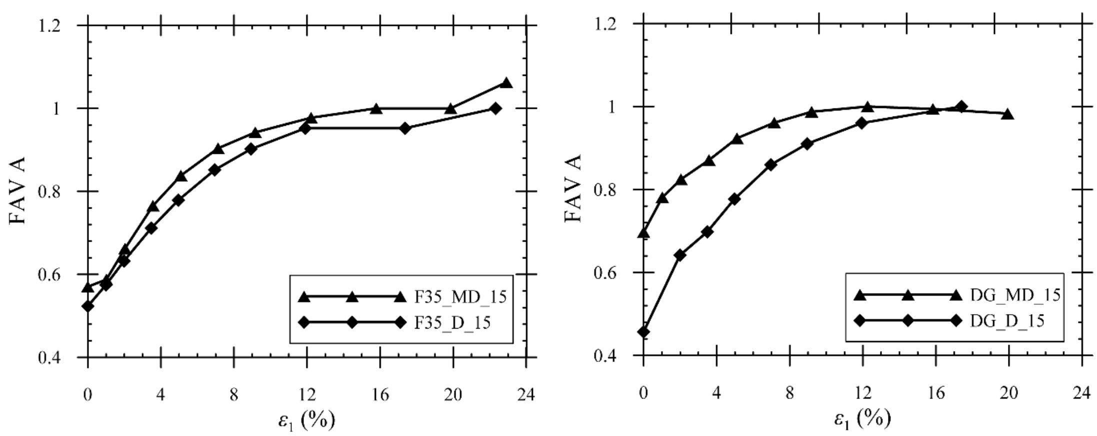

(a) F35 15KPa experiments (b) DG 15KPa experiments

Figure 22. Comparison between the evolution of FAV A versus ε_1 for (a) F35 15 kPa experiments and (b) DG 15 kPa experiments.

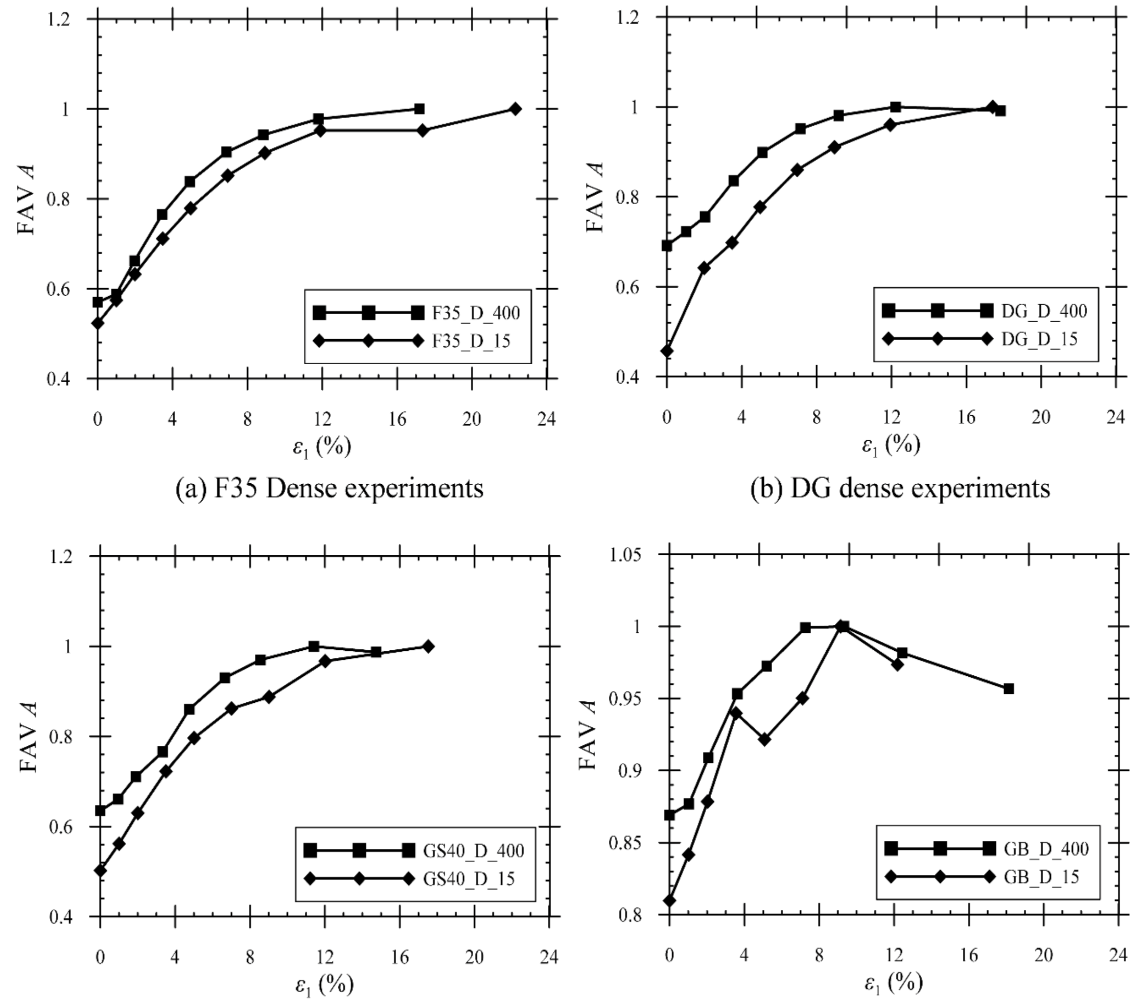

(a) F35 Dense experiments

(b) DG dense experiments

(c) GS40 dense experiments

(d) GB dense experiments

Figure 23. Comparison between the evolution of FAV A versus ε_1 for (a) F35 dense experiments, (b) DG dense experiments, (c) GS40 dense experiments, and (d) GB dense experiments.

Influence of Particle Morphology

The effect of morphology on initial fabric was assessed by comparing initial **F4** representation surfaces of dense 15 kPa experiments which were previously presented in Figure 20. Dense 15 kPa experiments were considered for comparison since a complete data set was acquired (i.e., scans for all tested materials) and the effect of σ_3 on initial isotropic fabric was minimal relative to experiments tested at 400 kPa confinement. Accordingly, it can be observed from Figure 20 that **F4** representation surfaces of F35_D_15 experiment were the closest to a spherical shape than other dense experiments tested at 15 kPa confinement. F35 sand was characterized earlier to have the highest sphericity index (i.e., most angular) of all granular materials tested in this study. The higher particle angularity led to a higher interlocking and more contacts between particles in random directions which produced a more isotropic distribution of contact normals. The influence of morphology on fabric evolution was also assessed in Figure 24 by comparing FAV A evolution of different materials (i.e., different morphology) tested at similar conditions (i.e., similar initial density state and σ_3). As illustrated in Figure 24, sands with similar initial density state and σ_3 exhibited similar fabric evolution that was higher (i.e., steeper in slope) than glass beads experiments. Glass beads were tested to provide baseline measurements of sphericity, roundness, and surface texture (i.e., almost perfect spheres with smooth surface texture). The absence of asperities and angularities in glass beads significantly reduced the interlocking between particles and so the resistance to fabric change as loading progressed. Therefore, a smaller change in FAV A was noticed for glass beads when compared to experiments on sands.

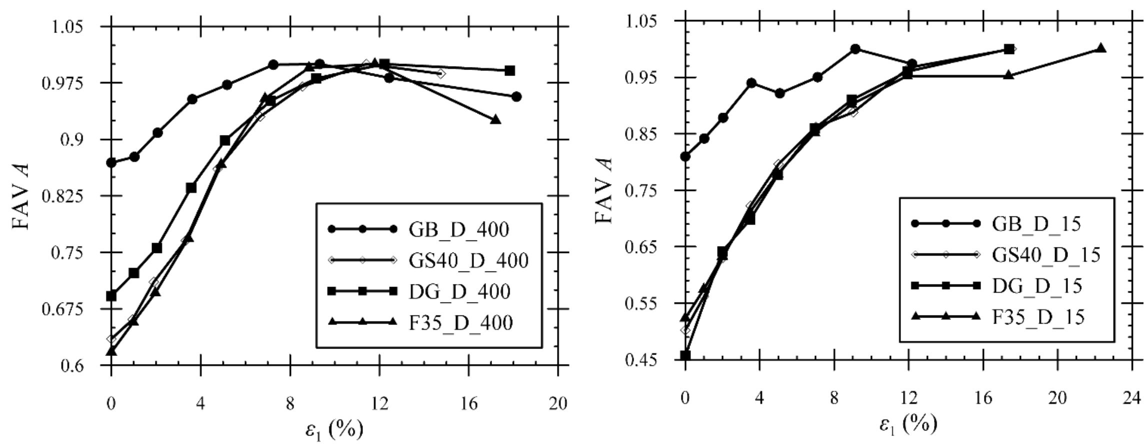

(a) D_400 specimens (b) D_15 specimens

Figure 24. Comparison between the eolution of FAV *A* versus ε_1 for (a) Dense 400 kPa experiments and (b) Dense 15 kPa experiments.

CHAPTER FOUR: CONCLUSIONS AND FUTUTRE RECOMENDATIONS

Conclusions

A series of triaxial compression experiments were conducted on four different granular materials while acquiring in-situ SMT scans. Experiments were conducted at two confining pressures and various density states while acquiring SMT scans at multiple axial strains. Images were processed and analyze to quantify microstructural variables such as contact normal vectors. The directional distribution of contact normals was analyzed and fabric tensors were calculated for each loading stage. The following conclusions were drawn:

1. The introduction of the distribution density term in fabric tensors of the second kind resulted in a better interpretation of the actual experimental data distribution than the conventional fabric tensor of the first kind. In other words, **F2** and **F4** fabric tensors better matched the 3D spherical histograms than **N2** and **N4** moment tensors, respectively.
2. A higher degree of estimate yielded a higher degree of fitting between fabric tensors and actual distributions of contact normals. In other words, 4^{th} order estimate of **F4** fabric tensors better matched the 3D spherical histograms than 2^{nd} order estimate of **F2** fabric tensors. Similarly, 4^{th} order estimate of **N4** moment tensors better matched the 3D spherical histograms than 2^{nd} order estimate of **N2** fabric tensors**.** Therefore, incorporating 4^{th} order tensors in micromechanical models will provide

a more accurate measurement of internal anisotropy than the conventional 2nd order tensors used in literature.

3. The directional distribution of global contact normals exhibited the highest degree of internal isotropy at initial configurations ($\varepsilon_1 = 0\%$).
4. As compression progressed, contact normals evolved (i.e., lined up) in the direction of compression resulting in a bias internal anisotropy toward the vertical applied global load.
5. Experiments were observed to approach a steady fabric that coincided with the critical state condition. This supports the Anisotropic Critical State Theory (ACST) which suggests that a constant critical state fabric must be satisfied in parallel with constant volume and deviatoric stresses for the critical state to occur.
6. A higher initial density state resulted in a higher degree of packing (i.e., more particles per volume) which generated more contacts that were more likely to be distributed randomly resulting in a higher degree of internal isotropy at initial configurations ($\varepsilon_1 = 0\%$). On the other hand, medium dense specimens included less particles and contacts; therefore, the deposition-induced preferential orientation of contact normals toward the vertical axis was remarkably inherited.
7. A lower confining pressure exposed less distortion on the ideal isotropic distribution of contact normals at initial configurations ($\varepsilon_1 = 0\%$). Accordingly, the initial directional distribution of contact normals showed a higher degree of internal isotropy for experiments tested at 15 kPa confining pressure compared with 400 kPa confinement.

8. Specimens failed via a single well-defined shear band (F35_D_400, GS40_D_400, and GB_D_400 experiments) showed vertical misalignment in the final **F4** representation surfaces toward the shear band direction. Conversely, a higher degree of vertical alignment was noticed in the final **F4** representation surfaces of experiments failed due to bulging which was attributed to the formation of multi-micro shear bands in opposite directions throughout the specimen.
9. Specimens tested at higher confining pressure and looser initial density state had higher FAV *A* values (i.e., higher degree of internal anisotropy). FAV *A* evolved approximately at the same slope regardless of the initial density state or the confining pressure.
10. A higher particle angularity led to a higher interlocking and more contacts between particles which produced a more random (i.e., isotropic) distribution of contact normals.
11. Tested sands with similar initial density state and confining pressure exhibited similar fabric evolution which was steeper in slope than glass beads experiments. This advocated the importance of morphology on fabric evolution.
12. Less particle asperities and angularities significantly reduced interlocking between particles and hence resistance to fabric change with respect to loading resulting in a lower degree of FAV *A* evolution.

Recommendations for Future Work

Fabric and its evolution were experimental quantified for granular assemblies in the course of conventional triaxial compression based on measurements of 3D contact normal vectors using high resolution SMT scans. 2nd and 4th order fabric tensors were successfully evaluated to experimentally validate theories and models that incorporate fabric as a state parameter. Particularly, FAV A evolution was quantified as an alternative for theoretical evolution implemented in the ACST. Furthermore, fabric will localize within regions inside the specimen body analogous to localization of shear (i.e., shear bands) and volume (i.e., void ratio) in conventional triaxial testing of granular material. As an attempt to investigate localized fabric, the single well-defined shear band (including part of surrounding volume) was extracted from the F35_D_400 scan near final loading stages and the same procedure was executed to construct fabric tensors. However, the sub-volume contained approximately 3000 particles which generated inadequate number of contact normals to quantify fabric tensors. Namely, 3D spherical histograms were observed to be highly discontinuous in random orientations and fitted smooth distribution density functions were assessed to be deceptive in describing localized fabric. In conclusion, scans on larger size specimens are required for the shear band to further extend; therefore, a statistically representative sample of 3D contact normal vectors can be analyzed and used to quantify localized fabric. As a motivation for this work, experiments conducted on the same type of material (i.e., same morphology) are expected to approach a unique localized fabric within evolved shear bands at the critical state condition as one would expect for volumetric state (i.e., void ratio) and stress state (i.e., critical state angle of friction).

LIST OF REFERENCES

Alshibli, K., Druckrey, A., Al-Raoush, R., Weiskittel, T., and Lavrik, N. (2014). "Quantifying Morphology of Sands Using 3D Imaging." *Journal of Materials in Civil Engineering*, 04014275.

Alshibli, K. A., Batiste, S. N., and Sture, S. (2003). "Strain localization in sand: plane strain versus triaxial compression." *Journal of Geotechnical and Geoenvironmental Engineering*, 129(6), 483-494.

Alshibli, K. A., Jarrar, M. F., Druckrey, A. M., and Al-Raoush, R. I. (2016). "Influence of Particle Morphology on 3D Kinematic Behavior and Strain Localization of Sheared Sand." *Journal of Geotechnical and Geoenvironmental Engineering*, 143(2), 04016097.

Amirrahmat, S., Alshibli, K. A., Druckrey, A. M., and Al-Raoush, R. I. (2017). "Micro Shear Bands: A Precursor for Strain Localization in Sheared Granular Materials."

ASTM, D. "4253 (2006) Standard test methods for maximum index density and unit weight of soils using a vibratory Table, ASTM International, West Conshohocken, PA."

ASTM, D. "4254 (2006) Standard test methods for minimum index density and unit weight of soils and calculation of relative density. ASTM International, West Conshohocken, PA."

Barreto, D., O'Sullivan, C., and Zdravkovic, L. (2009). "Quantifying the Evolution of Soil Fabric Under Different Stress Paths." *AIP Conference Proceedings*, 1145(1), 181-184.

Bathurst, R. J., and Rothenburg, L. (1990). "Observations on stress-force-fabric relationships in idealized granular materials." *Mechanics of materials*, 9(1), 65-80.

Calvetti, F., Combe, G., and Lanier, J. (1997). "Experimental micromechanical analysis of a 2D granular material: relation between structure evolution and loading path." *Mechanics of Cohesive-frictional Materials*, 2(2), 121-163.

Dafalias, Y. F. (2016). "Must critical state theory be revisited to include fabric effects?" *Acta Geotechnica*, 11(3), 479-491.

Dafalias, Y. F., and Manzari, M. T. (2004). "Simple plasticity sand model accounting for fabric change effects." *Journal of Engineering mechanics*, 130(6), 622-634.

Desrues, J., and Andò, E. (2015). "Strain localisation in granular media." *Comptes Rendus Physique*, 16(1), 26-36.

Desrues, J., Chambon, R., Mokni, M., and Mazerolle, F. (1996). "Void ratio evolution inside shear bands in triaxial sand specimens studied by computed tomography." *Géotechnique*, 46(3), 529-546.

Druckrey, A. M., Alshibli, K. A., and Al-Raoush, R. I. (2016). "3D characterization of sand particle-to-particle contact and morphology." *Computers and Geotechnics*, 74, 26-35.

Field, W. "Towards the statistics definition of a granular material." *Proc., Proc. 4th A. and NZ Conf. on Soil Mech.*, 143-148.

Fonseca, J., O'Sullivan, C., Coop, M. R., and Lee, P. D. (2013). "Quantifying the evolution of soil fabric during shearing using directional parameters." *Géotechnique*, 487-499.

Fu, P., and Dafalias, Y. F. (2015). "Relationship between void- and contact normal-based fabric tensors for 2D idealized granular materials." *International Journal of Solids and Structures*, 63(0), 68-81.

Guo, P. (2014). "Coupled effects of capillary suction and fabric on the strength of moist granular materials." *Acta Mechanica*, 225(8), 2261-2275.

Guo, P. J., and Stolle, D. F. (2005). "On the failure of granular materials with fabric effects." *Soils and foundations*, 45(4), 1-12.

Iwashita, K., and Oda, M. (1999). *Mechanics of granular materials: an introduction*, CRC Press.

Jang, D.-J., and Frost, J. D. (2000). "Use of image analysis to study the microstructure of a failed sand specimen." *Canadian geotechnical journal*, 37(5), 1141-1149.

Jiang, M., and Shen, Z. "Strength and fabric evolution of unsaturated granular materials by 3D DEM analyses." *Proc., AIP Conference Proceedings*, AIP, 273-276.

Kahn, J. S. (1956). "The analysis and distribution of the properties of packing in sand-size sediments: 1. On the measurement of packing in sandstones." *The journal of Geology*, 64(4), 385-395.

Kanatani, K.-I. (1984). "Distribution of Directional Data and Fabric Tensors." *Int. J. Engng Sci.*, 22(2), 149-164.

Kinney, J. H., and Nichols, M. C. (1992). "X-ray tomographic microscopy (XTM) using synchrotron radiation." *Annual review of materials science*, 22(1), 121-152.

Kuhn, M. R., Sun, W., and Wang, Q. (2015). "Stress-induced anisotropy in granular materials: fabric, stiffness, and permeability." *Acta Geotechnica*, 10(4), 399-419.

Lam, W.-K., and Tatsuoka, F. (1988). "Effects of initial anisotropic fabric and σ_2 on strength and deformation characteristics of sand." *Soils and Foundations*, 28(1), 89-106.

Li, B., and Zeng, X. (2014). "Effects of fabric anisotropy on elastic shear modulus of granular soils." *Earthq. Eng. Eng. Vib.*, 13(2), 269-278.

Li, X., and Dafalias, Y. (2011). "Anisotropic Critical State Theory: Role of Fabric." *Journal of Engineering Mechanics*, 138(3), 263-275.

Li, X., Yu, H. S., and Li, X. S. (2009). "Macro–micro relations in granular mechanics." *International Journal of Solids and Structures*, 46(25–26), 4331-4341.

Li, X. S., and Dafalias, Y. F. (2000). "Dilatancy for cohesionless soils." *Géotechnique*, 50(4), 449-460.

Li, X. S., and Dafalias, Y. F. (2002). "Constitutive Modeling of Inherently Anisotropic Sand Behavior." *Journal of Geotechnical and Geoenvironmental Engineering*, 128(10), 868-880.

Mehrabadi, M., and Cowin, S. (1978). "Initial planar deformation of dilatant granular materials." *Journal of the Mechanics and Physics of Solids*, 26(4), 269-284.

Mehrabadi, M., and Nemat-Nasser, S. (1981). "A micromechanical description of granular material behavior." *Journal of applied mechanics*, 48, 339.

Mehrabadi, M. M., Nemat-Nasser, S., and Oda, M. (1982). "On statistical description of stress and fabric in granular materials." *International Journal for Numerical and Analytical Methods in Geomechanics*, 6(1), 95-108.

Nemat-Nasser, S. (2000). "A micromechanically-based constitutive model for frictional deformation of granular materials." *Journal of the Mechanics and Physics of Solids*, 48(6–7), 1541-1563.

Nemat-Nasser, S., and Zhang, J. (2002). "Constitutive relations for cohesionless frictional granular materials." *International Journal of Plasticity*, 18(4), 531-547.

Ng, T.-T. (2009). "Discrete element method simulations of the critical state of a granular material." *International Journal of Geomechanics*, 9(5), 209-216.

Oda, M. (1972). "Initial fabrics and their relations to mechanical properties of granular material." *Soils and foundations*, 12(1), 17-36.

Oda, M. (1977). "Fabrics and their effects on the deformation behaviors of sand." *埼玉大学工学部建設系研究報告*, p1-59.

Oda, M., and Konishi, J. (1974). "Microscopic deformation mechanism of granular material in simple shear." *Soils and foundations*, 14(4), 25-38.

Oda, M., Nemat-Nasser, S., and Mehrabadi, M. M. (1982). "A statistical study of fabric in a random assembly of spherical granules." *International Journal for Numerical and analytical methods in Geomechanics*, 6(1), 77-94.

Oda, M., Takemura, T., and Takahashi, M. (2004). "Microstructure in shear band observed by microfocus X-ray computed tomography." *Géotechnique*, 54(8), 539-542.

Peña, A. A., Herrmann, H. J., and Lind, P. G. (2009). "Force chains in sheared granular media of irregular particles." *AIP Conference Proceedings*, 1145(1), 321-324.

Peters, J. F., Muthuswamy, M., Wibowo, J., and Tordesillas, A. (2005). "Characterization of force chains in granular material." *Physical Review E*, 72(4), 041307.

Qian, J.-g., You, Z.-p., and Huang, M.-s. (2013). "Anisotropic characteristics of granular materials under simple shear." *Journal of Central South University*, 20(8), 2275-2284.

Rivers, M. L. "tomoRecon: High-speed tomography reconstruction on workstations using multi-threading." 85060U-85060U-85013.

Rivers, M. L., Citron, D. T., and Wang, Y. "Recent developments in computed tomography at GSECARS." 780409-780409-780415.

Smith, W., Foote, P. D., and Busang, P. (1929). "Packing of homogeneous spheres." *Physical Review*, 34(9), 1271.

Taylor, J. M. (1950). "Pore-space reduction in sandstones." *AAPG bulletin*, 34(4), 701-716.

Theocharis, A., Vairaktaris, E., Fu, P., and Dafalias, Y. F. (2014). "Comparison of fabric tensors for granular materials." *Geomechanics from Micro to Macro*, K. Soga, K. Kumar, G. Biscontin, and M. Kuo, eds., CRC Press, 153-158.

Theocharis, A. I., Vairaktaris, E., Dafalias, Y. F., and Papadimitriou, A. G. (2016). "Proof of Incompleteness of Critical State Theory in Granular Mechanics and Its Remedy." *Journal of Engineering Mechanics*, 143(2), 04016117.

Tobita, Y. (1989). "Fabric tensors in constitutive equations for granular materials." *Soils and Foundations*, 29(4), 91-104.

Tong, Z., Fu, P., Zhou, S., and Dafalias, Y. F. (2014). "Experimental investigation of shear strength of sands with inherent fabric anisotropy." *Acta Geotechnica*, 9(2), 257-275.

Tordesillas, A., and Muthuswamy, M. (2009). "On the modeling of confined buckling of force chains." *Journal of the Mechanics and Physics of Solids*, 57(4), 706-727.

Wan, R. G., and Guo, P. J. (2004). "Stress dilatancy and fabric dependencies on sand behavior." *Journal of Engineering Mechanics*, 130(6), 635-645.

Winters, K. E., Taylor, O.-D. S., Berry, W. W., Rowland, W. R., and Antwine, M. D. (2016). "Cohesionless Soil Fabric and Shear Strength at Low Confining Pressures." *Geo-Chicago 2016*, 212-221.

Yang, Z., Lit, X., and Yang, J. (2008). "Quantifying and modelling fabric anisotropy of granular soils." *Géotechnique*.

Yimsiri, S., and Soga, K. (2001). "Effects of Soil Fabric on Undrained Behavior of Sands." *International Conferences on Recent Advances in Geotechnical Earthquake Engineering and Soil Dynamics*San Diego, CA.

Yimsiri, S., and Soga, K. (2010). "DEM analysis of soil fabric effects on behaviour of sand." *Géotechnique*, 483-495.

Zhao, J., and Guo, N. (2013). "Unique critical state characteristics in granular media considering fabric anisotropy." *Géotechnique*, 63(8), 695.

Zhu, H., Mehrabadi, M. M., and Massoudi, M. (2006). "Incorporating the effects of fabric in the dilatant double shearing model for planar deformation of granular materials." *International journal of plasticity*, 22(4), 628-653.

VITA

Wadi H. Imseeh was born in Jerusalem, State of Palestine. In summer 2015, he earned his Bachelor of Science Degree in Civil Engineering from Birzeit University, Palestine. Afterwards, he directly moved to The States for his graduate study. In fall 2015, he started his Ph.D. program in Geotechnology and Materials Engineering. Civil and Environmental Engineering Department, University of Tennessee, Knoxville, USA. He wrote this thesis in fall 2017 for his Master of Science Degree.